COMPENSATION OF FREQUENCY RESPONSE FUNCTION MEASUREMENTS BY INVERSE RCSA

by

Harsha Satyanarayana

A thesis submitted to the faculty of
The University of North Carolina at Charlotte
in partial fulfillment of the requirements
for the degree of Master of Science in
Mechanical Engineering

Charlotte

2017

Approved by:

_____
Dr. Tony Schmitz

_____
Dr. Gloria Elliott

_____
Dr. Joshua Tarbutton

ABSTRACT

HARSHA SATYANARAYANA. Compensation of frequency response function measurements by inverse RCSA (Under the direction of DR.TONY SCHMITZ)

.

The stability lobe diagram is a graphical device used to select stable cutting conditions in machining. The generation of the stability lobe diagram requires the tool-holder-spindle-machine frequency response function (FRF). Therefore, the accuracy of the stability lobe diagram depends on the accuracy of the measured FRF. Impact testing is a widely used technique to measure FRFs. Due to its setup simplicity, an accelerometer is often used to measure the structure's response that corresponds to the force impact. However, the use of an accelerometer causes mass loading, which leads to a shift in the measured natural frequency of the system.

The objective of this study is to understand the effect of accelerometer mass loading and cable damping on FRF measurements and to compensate it using the inverse receptance coupling substructure analysis (IRCSA) approach. Impact testing was completed for: 1) two steel rods of different diameters at multiple overhang lengths with clamped-free boundary conditions; and 2) two thin aluminum ribs of different lengths and thicknesses with clamped-clamped-clamped-free boundary conditions. The FRFs were measured using both accelerometers and a vibrometer, where the latter provided a non-contact measurement reference with no mass loading. Using IRCSA, a model of the accelerometer-cable FRF was decoupled from the measured FRF to compensate for mass loading and cable damping. The resultant IRCSA FRF was then compared against the

vibrometer FRF to verify the compensation technique. The natural frequency agreement after compensation was shown to be at the tenths of a percent level in all cases.

DEDICATION

I would like to dedicate my thesis to my loving parents, Vijayalakshmi and Satyanarayana, my sister Chethana, my guide, Dr. Tony Schmitz, and my friends.

ACKNOWLEDGEMENTS

First and foremost, I want to thank my advisor, Dr. Tony Schmitz, for providing me this opportunity. Without his assistance and dedicated involvement in every step throughout the process, this endeavour would have never been accomplished. I would like to thank him for his invaluable guidance and constant motivation. I would also like to thank the other members of the supervisory committee, Dr. Gloria Elliott and Dr. Joshua Tarbutton, for their participation.

I would also like to thank my lab mates and the students and faculty of the Mechanical Engineering and Engineering Science department that helped me in making this research possible.

Finally, I must express my very profound gratitude to my parents and my friends for providing me with unfailing support and continuous encouragement throughout my years of study and through the process of researching and writing this thesis. This accomplishment would not have been possible without them. Thank you.

TABLE OF CONTENTS

LIST OF FIGURES

LIST OF TABLES

CHAPTER 1: INTRODUCTION

One of the challenges during machining is to avoid chatter, a self-excited vibration. Chatter is caused by process instability and results in poor surface finish and low material removal rate. One of the ways to avoid chatter during machining is with the help of stability lobe diagrams. Figure 1.1 shows a schematic representation of an end milling operation where the axial depth of cut is denoted by b and spindle speed by Ω. For the operation to be stable at a given spindle speed the axial depth of cut should not exceed certain value. Stability lobe diagrams enable stable depth of cut and spindle speed combinations to be selected. Figure 1.2 shows the stability lobe diagram for a milling operation. Any region below the curve indicates stable cutting and the region above the line defines unstable cutting conditions

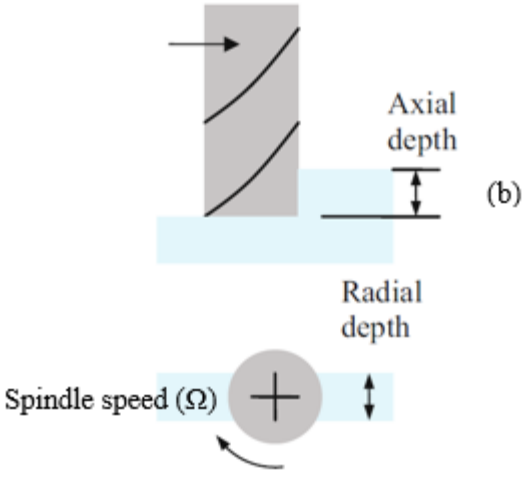

FIGURE 1.1. Schematic representation of a typical End milling operation [48].

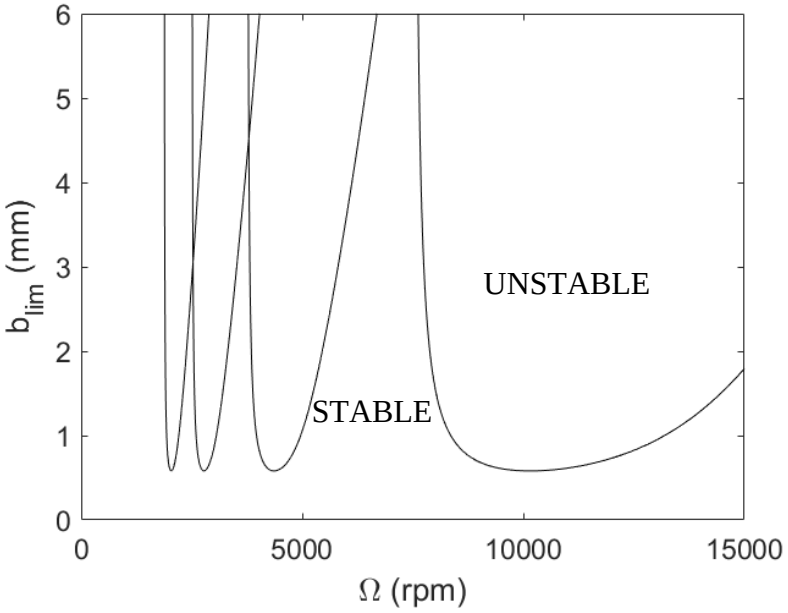

FIGURE 1.2. Stability lobe diagram of a milling process.

Although there are different methods to generate stability lobe diagram, all these methods require the tool point frequency response function (FRF), which provides the ratio of vibration response to a harmonic force input as a function of excitation frequency; see chapter 2 for additional discussion. FRFs can be determined experimentally by impact testing. This involves striking the tool with an impact hammer, which measures the force and recording the response with an accelerometer (contact measurement), laser vibrometer (non-contact measurement), or another transducer. Although it is known that accelerometer-based measurements have an inherent error source, the ease of setup for the accelerometer has made it a popular choice in industry. The error in the accelerometer measurements is due to the mass loading effect of the accelerometer and can be neglected if the modal mass of the tool is much larger than the mass of the accelerometer. However,

for small modal masses (such as a small diameter cutting tool), the mass loading error can cause a non-negligible frequency shift.

Figure 1.3 shows the comparison of the FRF obtained by an accelerometer and a laser vibrometer, which is non-contact and therefore does not include mass loading. It is seen that the accelerometer FRF is shifted by 123 Hz.

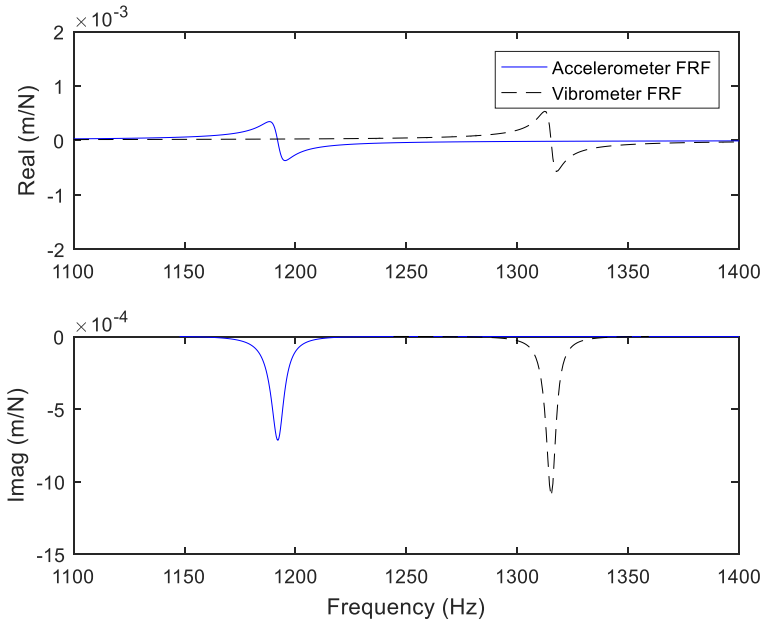

FIGURE 1.3. Accelerometer and vibrometer FRFs for 6.35 mm diameter rod with an overhang length of 55 mm.

The comparison of stability lobe diagram generated by FRFs from an accelerometer and vibrometer is presented in figure 1.4. It is seen that the stability lobe generated using the accelerometer-based FRF identifies different stable speeds and allowable depths of cut. Selecting cutting parameters using the mass loaded FRF can lead to unstable cutting conditions.

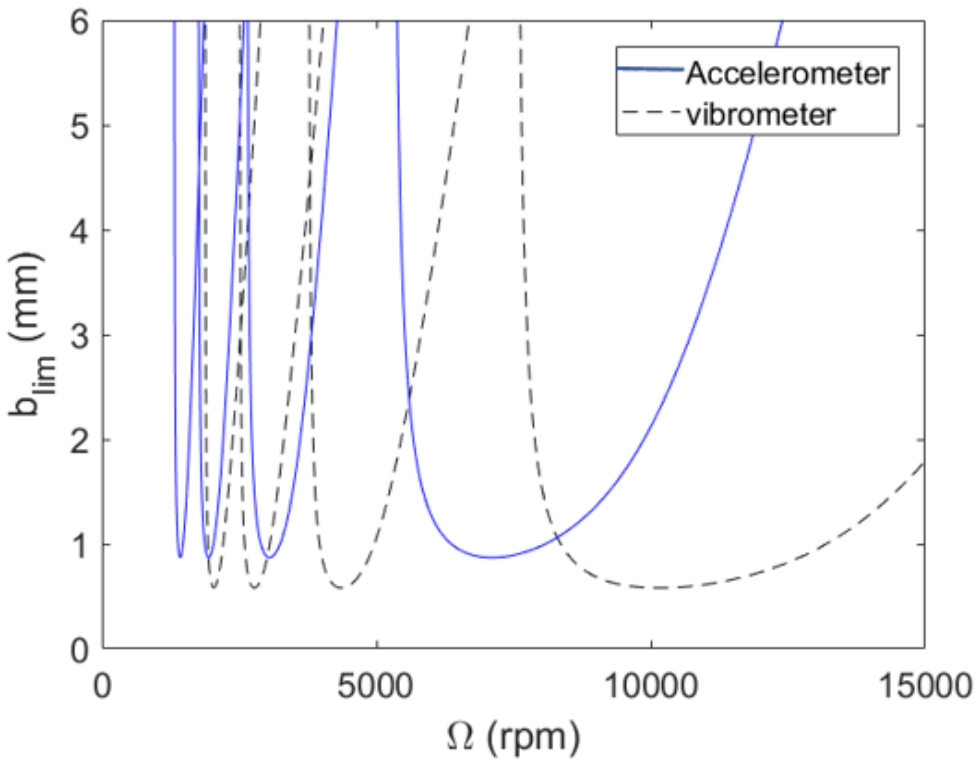

FIGURE 1.4. Comparison of stability lobe diagram generated using laser vibrometer and accelerometer FRFs.

The objective of this research is to compensate for the accelerometer mass loading effect and associated FRF frequency shift and magnitude change. Inverse receptance coupling substructure analysis (RCSA) is used to compensate the FRF.

CHAPTER 2: FREQUENCY RESPONSE FUNCTION

Consider a single degree of freedom, lumped parameter spring mass damper system as shown in figure 2.1, where m is the mass, k is the spring stiffness, c is the viscous damping coefficient, and x is the displacement. $Fe^{i\omega t}$ is the harmonic force applied to the spring mass damper, where t is the time and ω is the forcing frequency. The free body diagram is shown in figure 2.2, where $m\ddot{x}$ is the inertial force, $c\dot{x}$ is the damping force, and kx is the spring force.

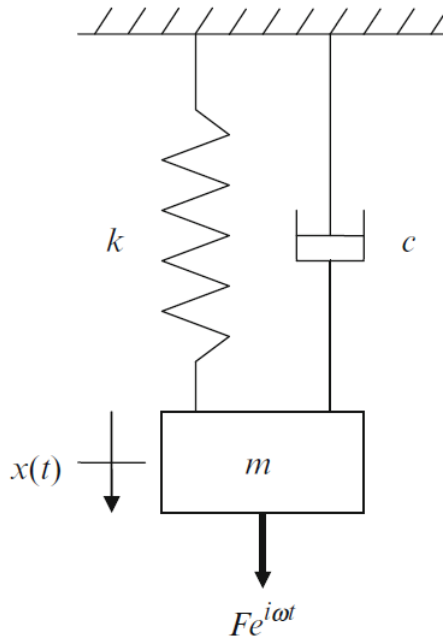

FIGURE 2.1. Spring-mass-damper model with harmonic input force [45].

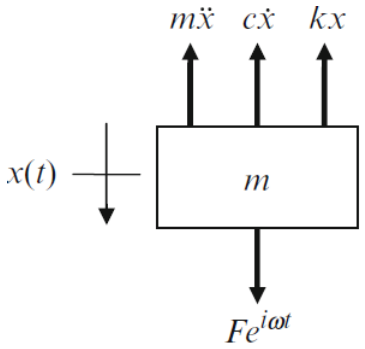

FIGURE 2.2. Free body diagram of spring-mass-damper system [45].

From the free body diagram, the equation of motion for the system can be written as,

$$m\ddot{x} + c\dot{x} + kx = Fe^{i\omega t}. \tag{2.1}$$

Equation (2.1) has both a homogenous and a particular solution. The homogenous solution $m\ddot{x} + c\dot{x} + kx = 0$ is the free vibration response and the particular solution represents the steady-state response (after the transient response attenuates). Given the force $f(t) = Fe^{i\omega t}$, the displacement can be written as $x(t) = Xe^{i\omega t}$, velocity as $\dot{x}(t) = i\omega Xe^{i\omega t}$, and acceleration as $\ddot{x}(t) = -\omega^2 Xe^{i\omega t}$. Substituting in equation (2.1) gives,

$$-m\omega^2 Xe^{i\omega t} + i\omega cXe^{i\omega t} + kXe^{i\omega t} = Fe^{i\omega t}. \tag{2.2}$$

Grouping and rearranging the terms yields,

$$\frac{X}{F}(\omega) = \frac{1}{-m\omega^2 + i\omega c + k}. \tag{2.3}$$

Equation (2.3) represents the frequency response function (FRF) for the model in figure (2.1).

$$\frac{X}{F}(\omega) = G(\omega) = \frac{1}{-m\omega^2 + i\omega c + k} \tag{2.4}$$

Using the relations $\frac{k}{m} = \omega_n^2$ (natural frequency), $\frac{c}{m} = 2\zeta\omega_n$ (ζ is the dimensionless damping ratio), and $r = \frac{\omega}{\omega_n}$ (frequency ratio), equation (2.4) is rewritten as:

$$G(r) = \frac{1}{k}\left(\frac{1}{(1-r^2)+i2\zeta r}\right). \tag{2.5}$$

Multiplying the numerator and denominator by the complex conjugate of the denominator gives,

$$G(r) = \frac{1}{k}\left(\frac{(1-r^2)-i2\zeta r}{(1-r^2)^2+(2\zeta r)^2}\right). \tag{2.6}$$

This equation contains both real and imaginary parts. The real part of the FRF is given by,

$$Re\big(G(r)\big) = \frac{1}{k}\left(\frac{(1-r^2)}{(1-r^2)^2+(2\zeta r)^2}\right). \tag{2.7}$$

The imaginary part of the FRF is given by,

$$Im\big(G(r)\big) = \frac{1}{k}\left(\frac{-i2\zeta r}{(1-r^2)^2+(2\zeta r)^2}\right). \tag{2.8}$$

If a constant force with zero frequency is applied, the system follows Hooke's law where the response is directly proportional to the magnitude of the force i.e., $F = kX$.

$$\frac{X}{F}(0) = G(0) = \frac{1}{k}\left(\frac{(1-(0)^2)-i2\zeta(0)}{(1-(0)^2)^2+(2\zeta(0))^2}\right) = \frac{1}{k}. \tag{2.9}$$

When the frequency of the force matches the natural frequency of the system, the frequency ratio is unity, $= 1$. By substituting in equations (2.7) and (2.8), $Re\big(G(r)\big) = 0$ and $Im\big(G(r)\big) = \frac{1}{2\zeta k}$ are obtained.

This can be observed in the typical FRF plots provided in figures 2.3 and 2.4.

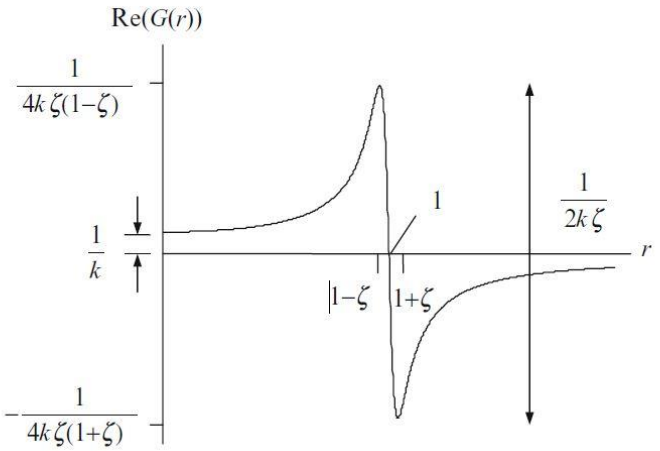

FIGURE 2.3. A typical plot of the real part of a single degree of freedom FRF versus *r* with key quantities identified [45].

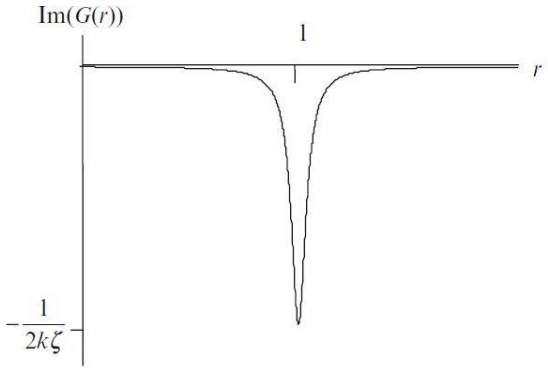

FIGURE 2.4. A typical plot of the imaginary part of a single degree of freedom FRF versus *r* with key quantifies identified [45].

Equation (2.5) can also be expressed in terms of magnitude and phase. The magnitude of the FRF is given by,

$$|G(r)| = \sqrt{(Re(G(r))^2 + (Im(G(r))^2} = \frac{1}{k}\sqrt{\frac{1}{(1-r^2)^2+(2\zeta r)^2}}. \qquad (2.10)$$

The phase provides a relationship between the real and imaginary parts of FRF. It also describes how much the system response lags the excitation. The phase is given by,

$$\phi(r) = tan^{-1}\left(\frac{Im(G(r))}{Re(G(r))}\right) = tan^{-1}\left(\frac{-2\zeta r}{1-r^2}\right). \quad (2.11)$$

The relation between real and imaginary parts, and the magnitude and phase is shown in figure (2.5).

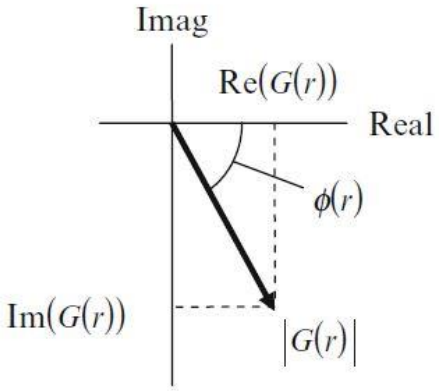

FIGURE 2.5. Vector representation of magnitude of FRF with phase angle [45].

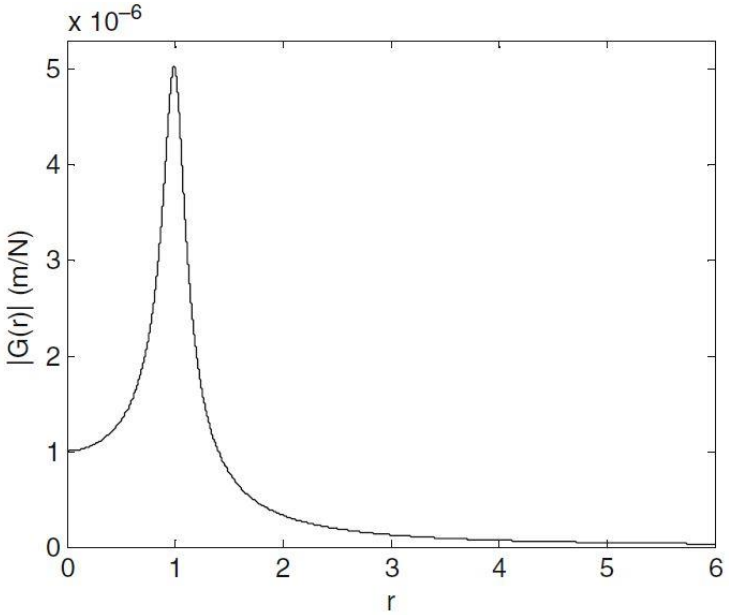

FIGURE 2.6. FRF magnitude versus *r* plot for a single degree of freedom system [45].

At zero frequency, the magnitude of the system response is equal to $\frac{1}{k}$. As shown in a FRF magnitude versus *r* plot (figure 2.6), when the excitation frequency becomes equal to the natural frequency of the system, $r = 1$, resonance is observed and the magnitude is maximum. As the excitation frequency increases above the natural frequency, the magnitude decreases.

As seen in figure 2.7, for the static condition where $r = 0$, the system response and the excitation force occur simultaneously (i.e., the phase is zero). The phase lag becomes $\frac{-\pi}{2}$ rad (90°) at $r = 1$, as illustrated in figure 2.8. As *r* becomes large, the phase lag approaches -π rad (180°).

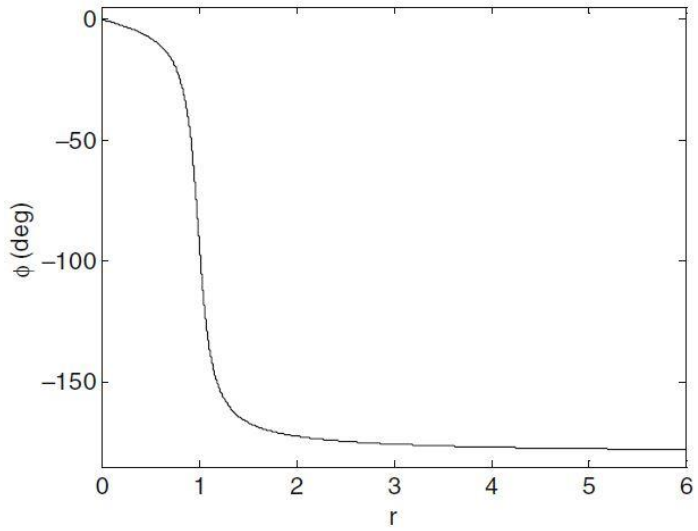

FIGURE 2.7. Phase versus *r* plot for a single degree of freedom system [45].

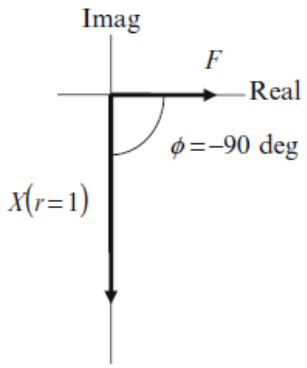

FIGURE 2.8. Vector representation of excitation and system response – the displacement lags the force by 90^0 for $r = 1$ [45].

CHAPTER 3: LITERATURE REVIEW

Receptance coupling is a method for predicting the FRF of an assembly by combining the FRFs of individual components. Substucturing has become a predominant technique in the analysis of the vibration characteristics of complex assemblies, where the assembly is separated into smaller components which are modelled individually and then analytically connected to form a complete model of the original assembly. Receptance coupling, first introduced by Bishop and Johnson in 1960 [1], has been an important tool in the study and prediction of vibrating systems. Since this early work, there has been a significant research done in the field. The following paragraphs summarize the relevant research and findings.

As mentioned in chapter 1, the FRF is a key input to stability lobe diagrams. The typical process of FRF generation requires an experimental measurement for each spindle-holder-tool combination. When a variety of tool-holder-spindle configurations are used in a machining facility, this method is time consuming and can be inaccurate if performed without adequate knowledge of dynamic testing procedures. To overcome this problem and to reduce the repetitive FRF tests for each tool-holder-spindle configuration, Schmitz used Receptance Coupling Substructure Analysis (RCSA) to predict tool point dynamics [2]. Schmitz et al. measured the FRF of the spindle-holder assembly and combined it with an analytical model of the tool FRF using RCSA. As the tool FRF was readily available from the analytical model, this method required only one FRF measurement at the holder free end to obtain the FRF of tool-holder-spindle assembly for different tool overhang lengths. Further, Schmitz et al. extended the concept of RCSA for chatter stability prediction during

high speed machining in milling [2-4]. Duncan et al. used RCSA to develop models for a stacked flexure setup and a spindle-holder-tool assembly to predict the interactions between the substructures and study the 'dynamic absorber effect' which would improve the dynamic stiffness of the assembly and critical stability limit and, therefore, increase the material removal rate in high speed machining. [5]. This work was further extended by Albertelli et al. [6]. The work done by Schmitz et al. [2-4] was refined by Kivanc et al. where the spindle-holder, tool, and the elements that connect the tool and holder were considered as three separated subsystems. A numerical beam model was suggested to evaluate the tool dynamics while a fitting procedure performed on experimental measurements was used to compute stiffness and damping coefficients of connecting elements [7].

Schmitz et al. initially considered only translational degrees of freedom and assumed rotational rigidity. Movahhedy et al. presented the importance of considering rotation dynamics and proposed a genetic algorithm to estimate tool holder connection parameters [8]. Park and Chae used finite element analysis and experimental techniques involving gauge tools to identify the rotational dynamics between substructures to improve the classic RCSA technique to identify the tool point receptance [9]. Further, Park et al. improved the ability of RCSA approach to predict the FRF of assemblies by including the rotational degrees of freedom at the joints in the assemblies. An algorithm was created to analytically extract the dynamics of the angular displacements from the linear cross and direct FRF measurements and these rotational dynamic parameters were included in generating the FRF of spindle-holder-tool assemblies [10]. This technique was adopted in other works [11]. Similar techniques where experiments with calibration tools were

performed to identify the rotational FRFs were also developed [12,13]. The application of RCSA in predicting torsional and axial receptances was also investigated by Schmitz [14].

Building on their previous work, Schmitz and Duncan developed a three component model which predicted tool point receptance by coupling modeled translational and rotational receptances (receptances of tool and extended holder) with that of standard measurements (receptances of the spindle holder base) using RCSA with the aim to perform just one experiment at the spindle-holder base and obtain the FRF at different overhang lengths. Schmitz and Duncan further extended the RCSA approach to coupling of holders enabling the use of different types of holders [15,16]. A modified version of this approach was proposed by Ahmadian et al. where the contacts between the substructures are coupled through continuous damped-elastic layer interfaces for a more realistic representation of the joint dynamics [17].

Namazi et al. modeled the holder-spindle taper contact by uniformly distributed translational and rotational springs to identify the contact stiffness and damping at the interface and coupled it with the holder-tool stick out which was modeled by Timoshenko beam elements using RCSA [18]. The effect of connection between components with coincident neutral axes on the receptance of the assembly was demonstrated by Schmitz et al. [19] who further extended the analysis by proposing a finite element modelling approach [20]. A new modelling technique based on the Timoshenko beam was proposed by Filiz et al. which limited both the modelling and computational efforts [21]. Erturk et al. combined RCSA and structural modification techniques to predict tool point FRF by modelling all the components of the spindle-holder-tool assembly using Timoshenko beam theory [22]. This technique was experimentally verified to efficiently predict chatter

stability when combined with the analytical stability lobe model put forth by Budak and Altintas [23,24]. Duarte et al. used a finite difference approach to obtain rotational dynamics in structural coupling analysis [25].

Rezaei et al. used a different approach based on RCSA to find the tool point FRF. Using inverse RCSA (IRCSA) the receptance of the tool was subtracted from the assembly receptance in order to obtain the receptance of the spindle and holder assembly [26]. This facilitated identification of the receptance of the new system when the tool was changed by finding the receptance of the changed tool analytically and coupling it with the spindle and holder assembly. Mehrpouya et al. investigated the deviations caused by the assumptions in IRCSA when used in joint dynamics modelling by comparing the results of a point mass model, a numerical approach, and experiments. The IRCSA proved to be very efficient requiring less computational efforts and experimentation to arrive at similar results [27]. Mehrpouya et al. further extended the inverse receptance coupling approach to a 3D model of tool-holder-spindle assembly with six degrees of freedom to obtain the FRFs of the joint between the substructures which would improve accuracy of modelling predictions [28].

Montevecchi et al. proposed a method based on IRCSA that requires FRF measurements of a single machine setup to obtain rotational responses that reduces the number of experiments required [29]. Matthias et al. proposed a technique that employs IRCSA to identify contact parameters at holder-tool interface using analytically calculated and experimentally obtained end point FRFs of the assembly at free-free end conditions [30].

Kumar et al. emphasized the importance of spindle-machine dynamics and compared three approaches to determine them. The predictions obtained by an analytical Euler-Bernoulli model fit to each mode was preferred over a finite difference approach based on multiple measurements as it required only one direct measurement at the free end of the spindle [31].

Erturk et al. studied the effects of bearing and interface dynamics on tool point FRF in spindle-holder-tool assemblies and observed that the variations in bearing dynamic properties affect the rigid body modes, variations in contact parameters of spindle-holder interface affect the first elastic mode, and the contact parameter variations in the holder-tool interface mainly affect the second elastic mode of the assembly. It was also observed that rotational dynamics are not negligible, but the average values of these properties at the interfaces can be used as they do not affect the tool point FRFs as much as the translational dynamics [32].

Yang et al. investigated the effect of collet geometry on the tool-point FRF predictions by modelling a spindle-holder-collet-tool assembly with two distributed joint interfaces of varying stiffness, collet-holder and collet-tool interfaces, and the dynamics of tool and collet were analyzed using Euler-Bernoulli beam theory. A computing procedure using RCSA was proposed to reduce the experimentation required to obtain the dynamics of spindle-holder assemblies of different sizes. This method reduced the prediction errors in natural frequencies to less than 5% for any collet geometry [33].

Tool point FRFs are generally identified in stationary conditions which results in reduced accuracy of chatter prediction techniques at high spindle speeds. To improve the

reliability of chatter prediction Grossi et al. presented a comprehensive experimental-analytical approach that allows to compute speed varying FRFs for a specific tool and then used a customized RCSA technique to predict speed varying tool tip FRFs of any other tools [34].

Zhang et al. proposed a new technique to use RCSA effectively to solve the constantly changing assembly responses in bi-rotary head five-axis machine tools in which a swivel model for holder tip receptances in swivel motion and a rotational model for the same in rotary motion were derived and then combined to get the tool point FRF at any posture of the bi-rotary head [35]. Apart from the modelling the tool pint FRFs, RCSA was also successfully utilized in a high-order position dependent dynamic modelling and analysis of ball screw feed drives in machine tools [36].

Yang et al. proposed a four component RCSA technique that included torsional and axial receptances along with bending receptances to develop a generalized method to predict and analyze tool point FRFs in milling, drilling, and boring operations [37]. RCSA proved very effective in obtaining tool point FRFs for chatter prediction in micro milling operations where the accurate measurement of tool tip dynamics is not possible through direct impact test measurements due to the miniature size of the tools. [38-41].

Although there are different methods to generate assembly receptances, at some point during the process it is necessary that at least one measurement be completed. This requires the conventional tests, such as the impact test discussed in chapter 4. These tests are generally carried out with the help of an accelerometer to measure the response of the system. As mentioned in chapter 1, the FRF measured using an accelerometer will have a

frequency shift due to mass loading of the structure by the addition of the accelerometer. In prior work, Ozsahin et al. [42] successfully compensated for the mass loading effect using the structural modification method put forward by Ozguven [43]. However, Ozahin et al. did not account for the mass of the cable, the mass of the adhesive holding the accelerometer, and the damping caused by the cable.

CHAPTER 4: RCSA

RCSA is used to predict an assembly's receptances by coupling receptances from the individual components. To predict the assembly receptance, the component receptances at the coupling location and the type of connection are needed. The connection between components can be rigid or flexible with or without energy dissipation (damping). An example for rigid coupling of two components is displayed in Fig. 4.1.

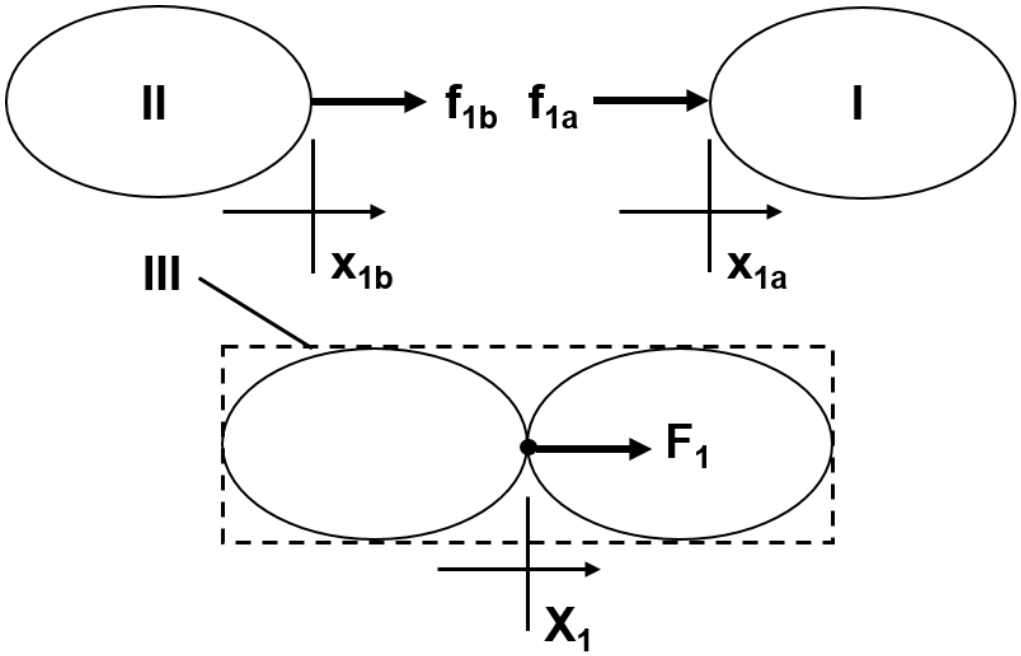

FIGURE 4.1. Two component RCSA model: I and II are individual components and III is the assembly. Component coordinates and forces are lower case; assembly coordinates and forces are upper case [47].

For this example, the direct receptance of component I can be described as

$$h_{1a1a} = \frac{x_{1a}}{f_{1a}} \tag{4.1}$$

and the direct receptance of component II can be described as

$$h_{1b1b} = \frac{x_{1b}}{f_{1b}}. \tag{4.2}$$

The compatibility condition for rigid coupling is given by Eq. 4.3 and substituting for displacements from Eq. 4.1 and Eq. 4.2 results in Eq 4.4.

$$x_{1a} - x_{1b} = 0 \tag{4.3}$$

$$h_{1b1b}f_{1b} - h_{1a1a}f_{1a} = 0 \tag{4.4}$$

The equilibrium condition, $f_{1a} + f_{1b} = F_1$, relates the internal (component, lower case variable) forces to the external (assembly, upper case variable) forces. Using this condition and solving for f_{1b} results in Eq 4.5, which is rearranged in Eq. 4.6.

$$h_{1b1b}f_{1b} - h_{1a1a}F_1 + h_{1a1a}f_{1b} = 0 \tag{4.5}$$

$$f_{1b} = (h_{1a1a} + h_{1b1b})^{-1}h_{1a1a}F_1 \tag{4.6}$$

Substituting for f_{1b} in the equilibrium condition and solving for f_{1a} gives

$$f_{1a} = (1 - (h_{1a1a} + h_{1b1b})^{-1}h_{1a1a})F_1. \tag{4.7}$$

Using these equations, the assembly (III) direct receptance, H_{11}, at assembly coordinate X_1 can be expressed as shown in Eq. 4.8.

$$H_{11} = \frac{X_1}{F_1} = \frac{x_{1a}}{F_1} = \frac{h_{1a1a}f_{1a}}{F_1} = h_{1a1a} - h_{1a1a}(h_{1a1a} + h_{1b1b})^{-1}h_{1a1a} \tag{4.8}$$

4.1. Inverse RCSA approach for mass loading compensation

A tool point FRF may be measured by impact testing; see chapter 5 for more information. The experimental FRF differs, at some level, from the actual FRF due to the accelerometer and cable mass for this contact-type measurement. A reduction in the natural

frequency(s) and FRF magnitude may be observed, depending on the amount of mass loading and its ratio to the modal mass(es) for the system under test.

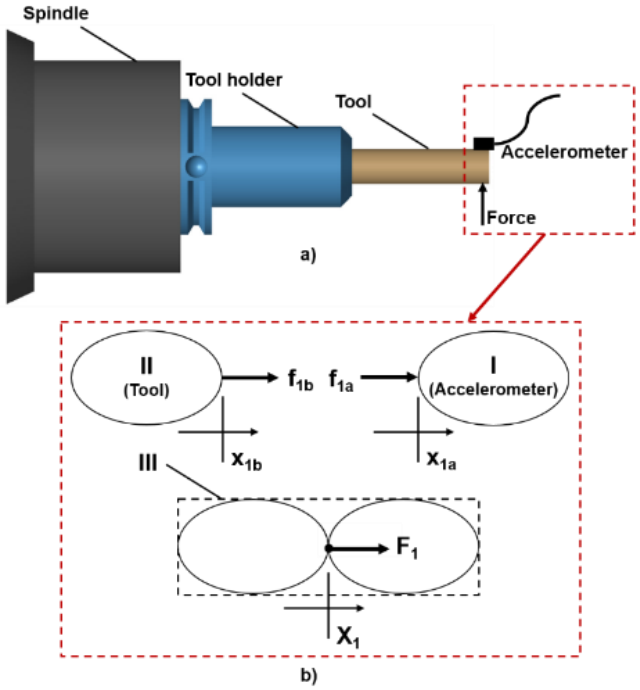

FIGURE 4.2. a) FRF measurement b) RCSA model [47].

The accelerometer-cable mass can be compensated using inverse RCSA, where the corresponding RCSA model is depicted in Fig. 2b. In this model, it is assumed that the accelerometer is rigidly coupled to the tool point (using modal wax or other connection strategy). The measurement provides the assembly receptance, $H_{11} = \frac{X_1}{F_1}$. The accelerometer-cable receptance is $h_{1a1a} = \frac{x_1}{f_1}$, while the unknown tool point receptance is $h_{1b1b} = \frac{x_2}{f_2}$. The tool point receptance can be determined by rearranging Eq.4.7 as shown in Eq. 4.8. This approach is referred to as inverse RCSA since Eq. 4.9 represents a decoupling, rather than a coupling, operation.

$$h_{1b1b} = -h_{1a1a} + h_{1a1a}(h_{1a1a} - H_{11})^{-1} h_{1a1a} \qquad (4.9)$$

For mass compensation only (i.e., mass loading of the structure under test by the accelerometer-cable), the accelerometer-cable may be defined as a point mass. The corresponding receptance (m/N) is provided in Eq. 4.10, where m is the mass (kg) and ω is the frequency (rad/s).

$$h_{1a1a} = \frac{-1}{m\omega^2} \tag{4.10}$$

However, when there is a decrease in the measurement magnitude due to cable energy dissipation, then it becomes necessary to compensate for the damping. For this study, a viscous damping model is considered and Eq. 4.10 can be rewritten as to include the viscous damping coefficient, c.

$$h_{1a1a} = \frac{-1}{m\omega^2 + ic\omega} \tag{4.11}$$

CHAPTER 5: MEASUREMENT TECHNIQUE

As mentioned in chapter 1, impact testing may be used to determine the FRF of a structure. In this approach, an impact hammer is used to apply a force impulse, excite the structure over a broad range of frequencies, and record the applied force. A transducer is used to record the vibration response of the structure. The time domain response from the hammer and the transducer is input to a dynamic signal analyzer (DSA), which computes the Fourier transform of these signals to convert them into the frequency domain. The DSA then calculates the ratio of frequency domain vibration signal to the frequency domain force signal to give the FRF. Figure 5.1 shows a schematic of the FRF measurement. Here, $f(t)$ is the hammer force and $x(t)$, $\dot{x}(t)$, and $\ddot{x}(t)$ are the displacement, velocity or acceleration depending on the type of transducer used.

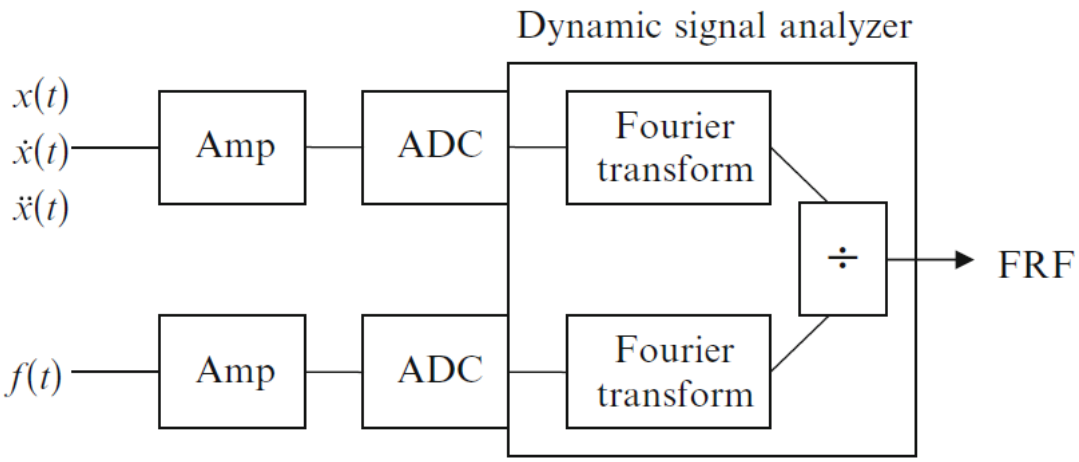

FIGURE 5.1. Schematic of FRF measurement setup [45].

5.1. Impact hammer

Impact hammers consists of a force sensor, located behind the tip of the hammer, which measures the force input during the hammer strike. The tip of the hammer may be soft or stiff depending on the desired frequency range. Hard plastic and metal tips with higher stiffness are used to excite a larger frequency range, while softer rubber tips are used to excite a lower frequency range. The energy input given to the structure is also a function of the hammer mass. Therefore, hammers are available in different size. An example of different hammer sizes is show in figure 5.1.1.

FIGURE 5.1.1. Example of impact hammers [45].

5.2. Accelerometer

An accelerometer measures the vibration response by generating a signal proportional to the acceleration of the structure. An accelerometer consists of a seismic mass and a piezoelectric material which produces a charge when strained. This accelerometer is mounted on the structure as shown in figure 5.2.1. When the structure moves, the seismic mass applies an inertial force on the piezoelectric material which strains the material and produces a charge. The charge is proportional to the acceleration and the corresponding voltage is used as the measurement signal.

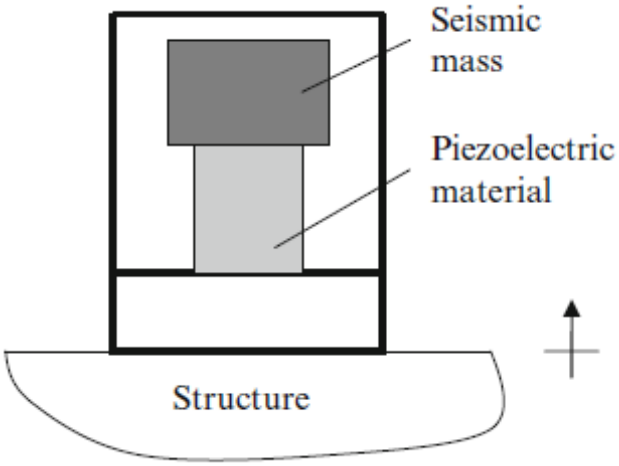

FIGURE 5.2.1. Schematic representation of an accelerometer [45].

The DSA receives acceleration (A) of the structure and excitation force (F) as input. It calculates the frequency domain ratio $\frac{\mathrm{A}}{F}(\omega)$, referred to as inertance or accelerance. If $x(t) = Xe^{i\omega t}$ represents the displacement of harmonic vibration, then the acceleration is given by $\ddot{x}(t) = (i\omega)^2 Xe^{i\omega t} = -\omega^2 Xe^{i\omega t}$. Using this relation, the conversion from accelerance, $\frac{\mathrm{A}}{F}(\omega)$, to receptance, $\frac{\mathrm{X}}{F}(\omega)$, is

$$\frac{X}{F}(\omega) = \frac{X}{A}\frac{A}{F} = -\frac{1}{\omega^2}\frac{A}{F}. \quad (5.2.1)$$

FIGURE 5.2.2. Different sizes of accelerometer [45].

5.3. Laser Vibrometer

A laser vibrometer is a non-contact type vibration measuring instrument which works on the principle of the Doppler shift. The operation is shown in figure 5.3.1. A laser beam with a single frequency f_0 is emitted by the laser head. This beam is passed through a beam splitter, which redirects a portion of the light towards the photo detector to serve as a reference beam and the rest continues towards the acoustic-optic modulator (AOM) which upshifts the laser to a frequency $f_0 + f_1$. When the light from the AOM strikes the moving target surface and is reflected back, it is Doppler shifted and the shift is directly proportional to the velocity. This frequency shifted light is recombined with the refence

light at the photo detector and the current from the photo detector is used to determine the time-dependent target velocity. This signal is then passed to the DSA.

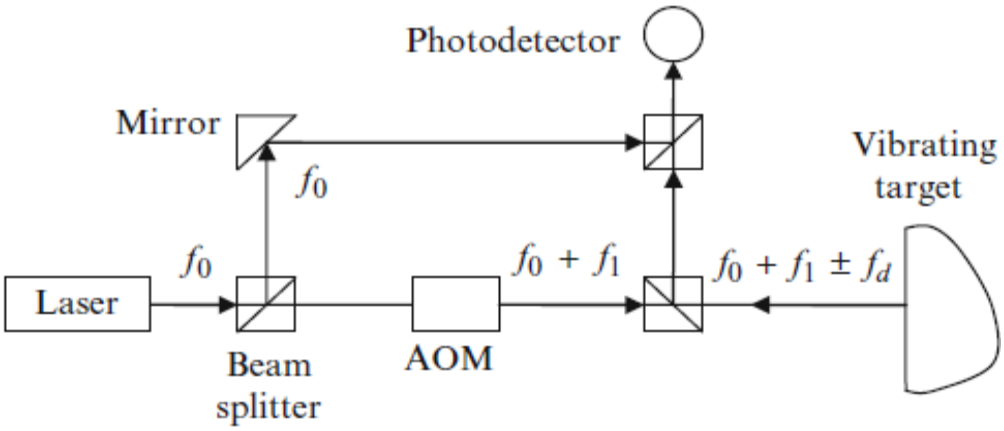

FIGURE 5.3.1. Laser vibrometer schematic [45].

Similar to the accelerometer, the DSA receives the velocity (V) of the structure and the excitation force (F) as input. The DSA calculates the frequency domain ratio $\frac{\mathrm{V}}{F}(\omega)$, referred to as mobility. If $x(t) = Xe^{i\omega t}$ represents the displacement of harmonic vibration, then the velocity is given by $\dot{x}(t) = i\omega Xe^{i\omega t}$. Using this relation, the conversion from mobility, $\frac{\mathrm{V}}{F}(\omega)$, to receptance, $\frac{\mathrm{X}}{F}(\omega)$, is

$$\frac{X}{F}(\omega) = \frac{X}{V}\frac{V}{F} = \frac{1}{i\omega}\frac{V}{F}. \tag{5.3.1}$$

5.3.1. FRF phase correction

When using a laser vibrometer for FRF measurements, a time delay between the measured response and the actual system response can be introduced by the signal conditioning electronics that convert the incoming optical signal into a voltage proportional to velocity. Figure 5.3.1.1 shows a sample time delay between the actual (blue line) and measured (red line) vibration response.

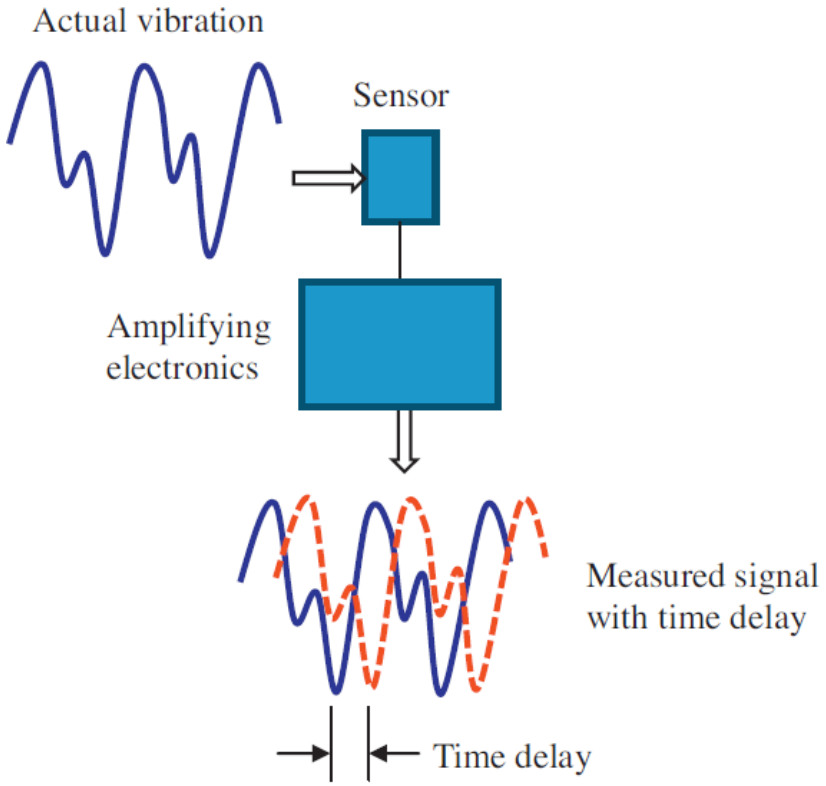

FIGURE 5.3.1.1. Representation of time delay between actual and measured vibration signal [46].

Schmitz and Ganguly studied this time delay when using a capacitive sensor [46] and pointed out that a constant time delay results in a phase error which increases linearly with increasing frequency. Figure 5.3.1.2 show the phase error of {-18, -36, and -54} deg for oscillating frequencies of {1, 2, and 3} Hz with a 50 ms time delay; x_a and x_m represent the actual and measured signals, respectively.

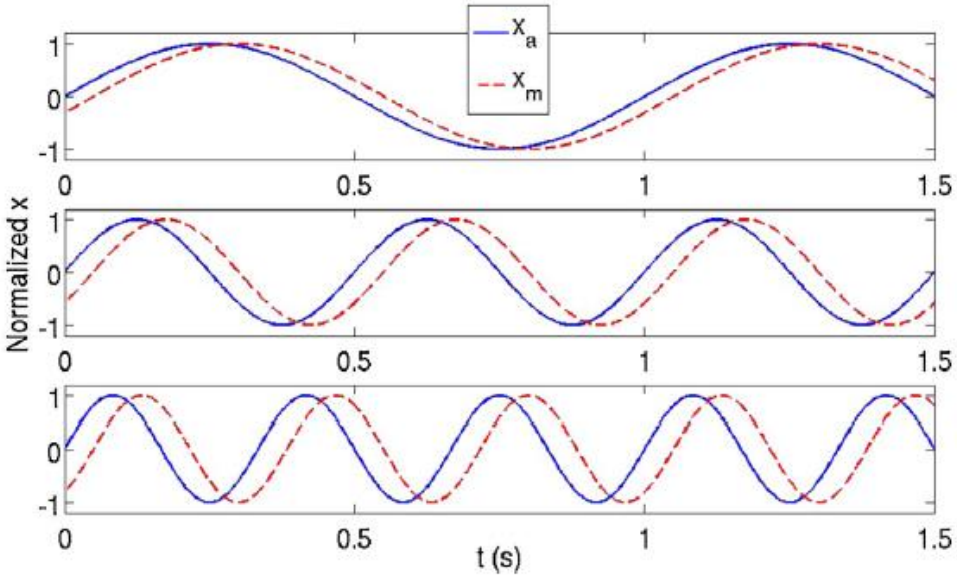

FIGURE 5.3.1.2. Effect of frequency on phase for a fixed time delay [46].

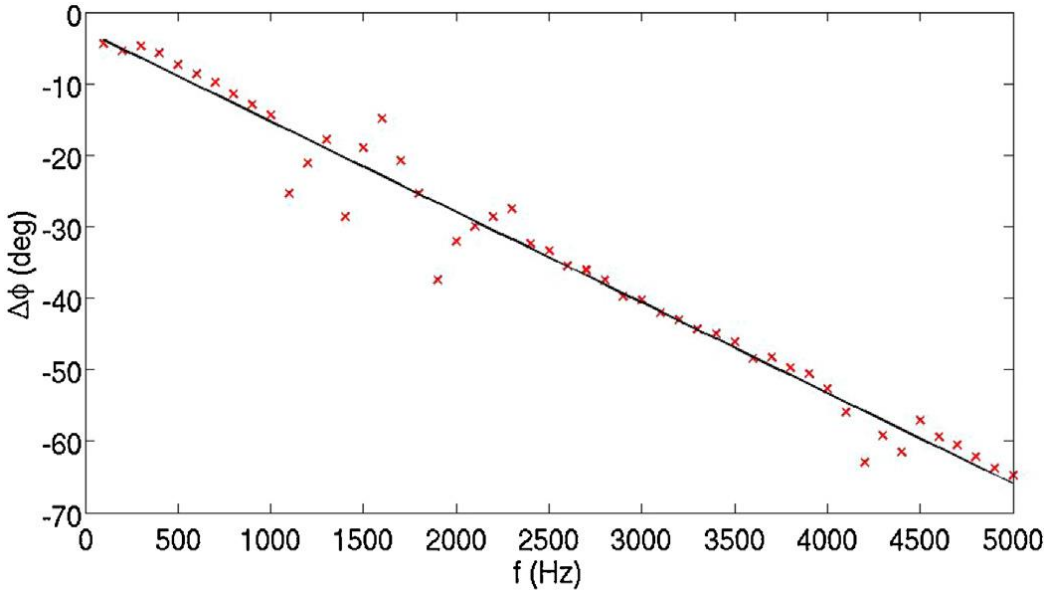

FIGURE 5.3.1.3. Phase error between accelerometer and the capacitive sensor [46].

Figure 5.3.1.3 shows the frequency-dependent phase error for a constant time delay between two sensors, an accelerometer and a capacitive sensor, as reported in [46]. The

phase error is calculated using $\Delta\Phi f = cos^{-1}(\frac{x_a x_m}{|x_a||x_m|})$. The slope of the best fit line in the figure is -12.9 deg/kHz. The effect of the time delay can be removed by subtracting the phase error ΔΦ, which is a product of the slope (s) and frequency (f), from the measured phase (Φ_m). The corrected phase, $\Phi_c = \Phi_m - \Delta\Phi = \Phi_m - sf$, is used to modify the real and imaginary parts of the FRF. This compensation strategy was applied in this research.

CHAPTER 6: EXPERIMENTAL SETUP

The tool point FRF is a measure of the vibration response of the tool to a harmonic force input as a function of excitation frequency

$$H(\omega) = \frac{X(\omega)}{F(\omega)}, \tag{6.1}$$

where $X(\omega)$ and $F(\omega)$ are the discrete Fourier transforms of the vibration response and input force signals. This tool point FRF can be obtained by using impact test as explained in chapter 5. When measuring the FRF of a tool using an accelerometer, there is a frequency shift due to the mass loading effect of the accelerometer. This effect is significant when the structural modal mass is small, such as small diameter cutting tools. To correct this mass loading effect, a model of the accelerometer FRF is subtracted from the experimental FRF (measured with the accelerometer) using the inverse RCSA method described in chapter 4. This decoupling is represented by Eq. 6.2,

$$h_{1b1b} = -h_{1a1a} + h_{1a1a}(h_{1a1a} - H_{11})^{-1} h_{1a1a}, \tag{6.2}$$

where $h_{1b1b} = \frac{x_{1b}}{f_{1b}}$ is the compensated tool point receptance, $H_{11} = \frac{X_1}{F_1}$ is the mass loaded assembly receptance (measured), and $h_{1a1a} = \frac{x_{1a}}{f_{1a}}$ is the analytical accelerometer-cable receptance. The accelerometer-cable receptance is modeled using Eq 6.3 (no damping) or Eq. 6.4 (with damping), where *m* is the mass (kg), *c* is the viscous damping coefficient (N-s/m), and ω is the forcing frequency (rad/s).

$$h_{1a1a} = \frac{1}{-m\omega^2} \tag{6.3}$$

$$h_{1a1a} = \frac{1}{-m\omega^2 + ic\omega} \tag{6.4}$$

Two different setups were used to perform the experiments. The first setup had a 12.7 mm diameter steel rod clamped onto an aluminum base with a split clamp as shown in figure 6.1. The second setup, shown in figure 6.2, had a 6.35 mm diameter steel rod clamped in an ER 16 collet holder with a CAT-40 spindle interface. For this study, the collet was secured in a spindle nose attached to a large steel block (i.e., the spindle test stand) using a manual draw bolt. Both rods had clamped-free boundary conditions.

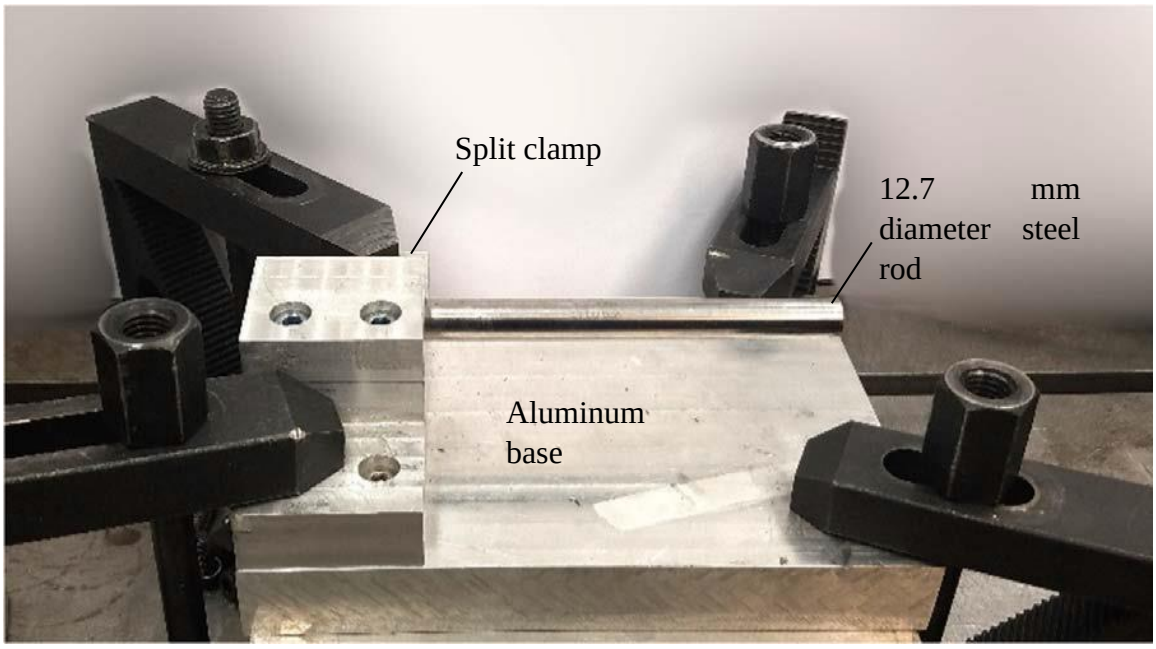

FIGURE 6.1. 12.7 mm diameter steel rod setup.

Impact testing was performed at multiple overhang lengths for both rods using a miniature modal hammer (PCB 084A17) with a steel tip. Two accelerometers, a medium size

accelerometer (PCB 352A21) and a small size accelerometer (PCB 352C23), were attached to the free end of the rods to measure their vibration responses.

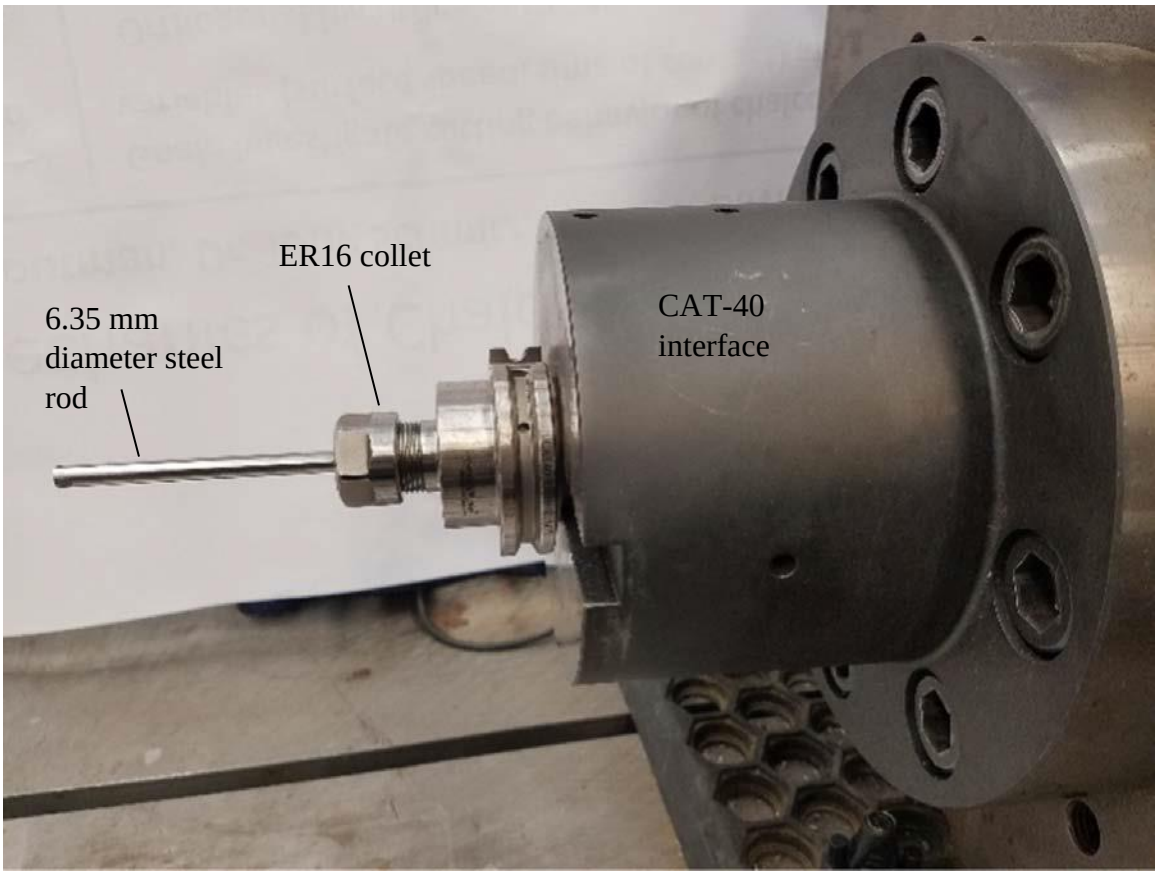

FIGURE 6.2. 6.35 mm diameter steel rod setup.

An Ohaus AV264C Adventurer ProAnalytical Balance (0.1 mg resolution) was used to measure the accelerometer-cable masses. A laser vibrometer (Polytec OFV-534) was used to provide a non-contact measurement reference with no mass loading. The laser vibrometer was set up such that the laser beam pointed at the same location where the accelerometer was attached. It was placed at a stand-off distance of approximately 300 mm, which is in accordance with the standard specified by the manufacturer.

TXF™, a commercial software, served as the dynamic signal analyzer. The time delay that arises due to lack of synchronization between the measured response and the actual system response induced a frequency dependent phase error into the FRF for the vibrometer measurements. The phase correction algorithm explained in chapter 5 was used to remove this phase error from the FRF.

6.1. Experimental procedure:

The outline of the experimental procedure follows.

Step 1: The small accelerometer was attached to the free end of the rod with modal wax and the cable was secured to prevent any external disturbances of the cable from reaching the accelerometer end.

Step 2: Impact testing was performed on the rod using the miniature modal hammer. The vibration response of the rod as measured by the accelerometer was recorded and processed by TXF™ to output the FRF.

Step 3: The accelerometer was removed from the rod and the laser vibrometer was switched on. The rod is struck by the same hammer again and the vibration response of the system as measured by the laser vibrometer was recorded and processed by TXF™ to output the FRF. This receptance was compensated for phase error.

Step 4: The accelerometer-cable receptance, based on the mass, was obtained analytically.

Step 5: Using IRCSA, the mass loading effect of the accelerometer was removed by subtracting the accelerometer-cable receptance from the receptance of rod measured by the accelerometer; see chapter 4 for more details.

Step 6: The mass loading correction was validated by comparing the IRCSA rod receptance to the rod receptance measured by the laser vibrometer.

Step 7: The medium accelerometer was then attached to the rod as described in step 1. The same procedure, from step 2 through step 6, was repeated.

This experimental procedure was followed for four different cases to validate the mass loading correction and to understand the damping effect caused by the accelerometer cable. These cases are described in the following sections.

6.2. Case 1: 12.7 mm rod with clamped-free boundary condition

The 12.7 mm diameter steel rod was secured with a split clamp onto an aluminum base which was, in turn, attached to a workbench using toe clamps. This represents a clamped-free boundary condition. The accelerometers, one at a time, were attached to the free end of the rod using modal wax and the cable was taped down to the aluminum base as shown in the figure 6.2.1.

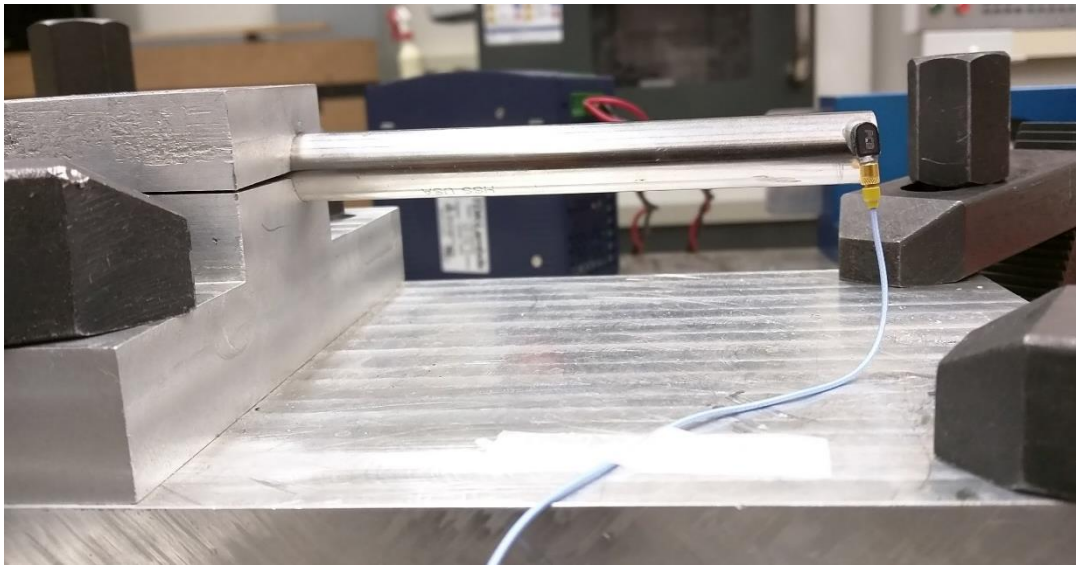

FIGURE 6.2.1. Small accelerometer attached to the 12.7 mm diameter rod using modal wax.

The experiments were then carried out at three different overhang lengths, 102 mm, 111 mm, and 124 mm, to obtain the receptance measurements and the results were analyzed.

6.3. Case 2: 6.35 mm rod with clamped-free boundary condition

The 6.35 mm diameter steel rod was clamped in an ER 16 collet holder that was secured in the spindle test stand with a CAT-40 interface using a manual draw bolt. This approximately represents a clamped-free boundary condition. The accelerometers, one at a time, were attached to the free end of the rod using modal wax and the cable was taped down to the workbench supporting the setup as shown in figure 6.3.1.

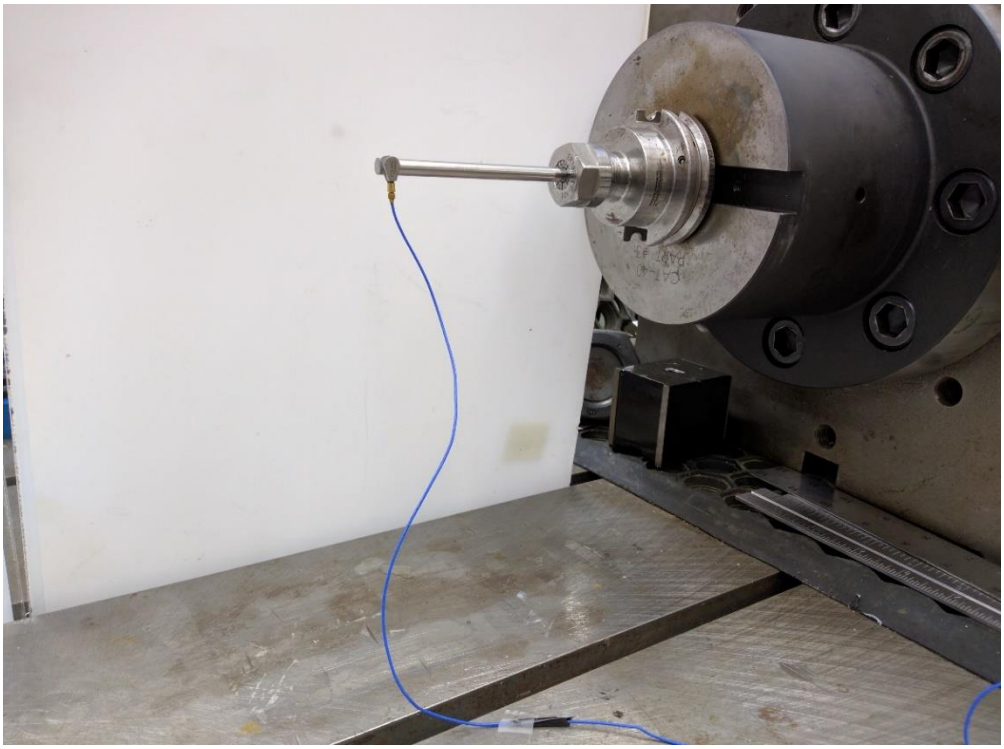

FIGURE 6.3.1. Medium accelerometer attached to the 6.35 mm diameter rod using modal wax.

The experiments were then carried out at two different over hang lengths of 79 mm and 89 mm to obtain the receptance measurements and the results were analyzed.

6.4. Case 3: 6.35 mm rod with clamped-free boundary condition without accelerometer cable

The accelerometers, one at a time, were attached to free end of the 6.35 mm diameter rod using modal wax. The cable was disconnected from the accelerometer. The accelerometers were not used to record the measurements, but just to simulate the mass loading effect. The experiments were then carried out at two different overhang lengths, 79 mm and 89 mm. The laser vibrometer was used to record the FRFs with and without the accelerometer as shown in figure 6.4.1. The results were then compared with the measurements from case 2 to determine if the cable had a damping effect on the rod.

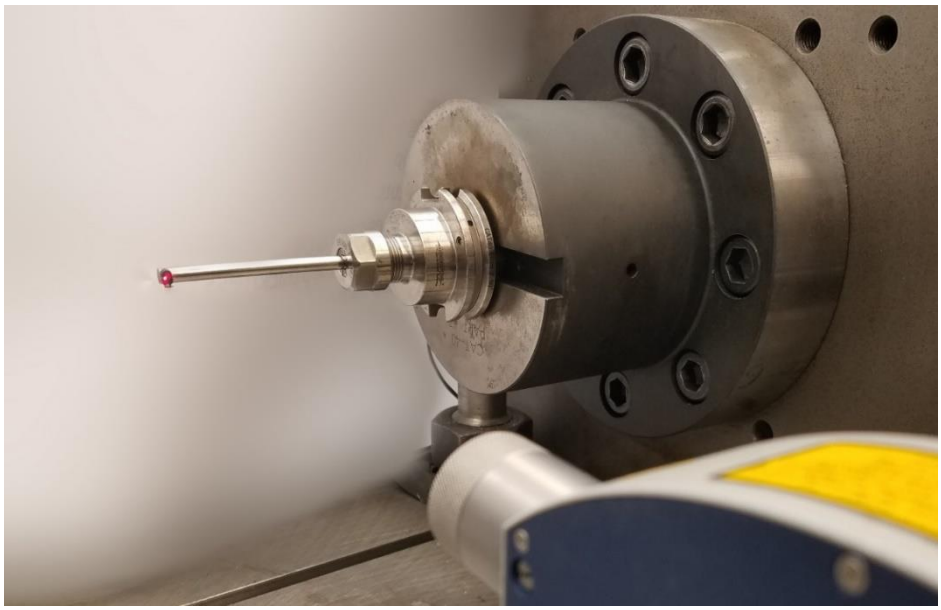

FIGURE 6.4.1. Small accelerometer attached to the 6.35 mm diameter rod using modal wax.

6.5. Case 4: 6.35 mm rod with clamped-free boundary condition and varying accelerometer cable length

The accelerometers, one at a time, were attached to free end of the 6.35 mm diameter rod using modal wax. The cable was supported by a miniature metal stand as shown schematically in figure 6.5.1. The experiments were then carried out for two different overhang lengths of the rod, 55 mm and 65 mm, with three different catenary lengths of the cable, i.e., 304 mm, 608 mm and 912 mm, to understand the dependence of cable length on the damping effect of cable on the rod.

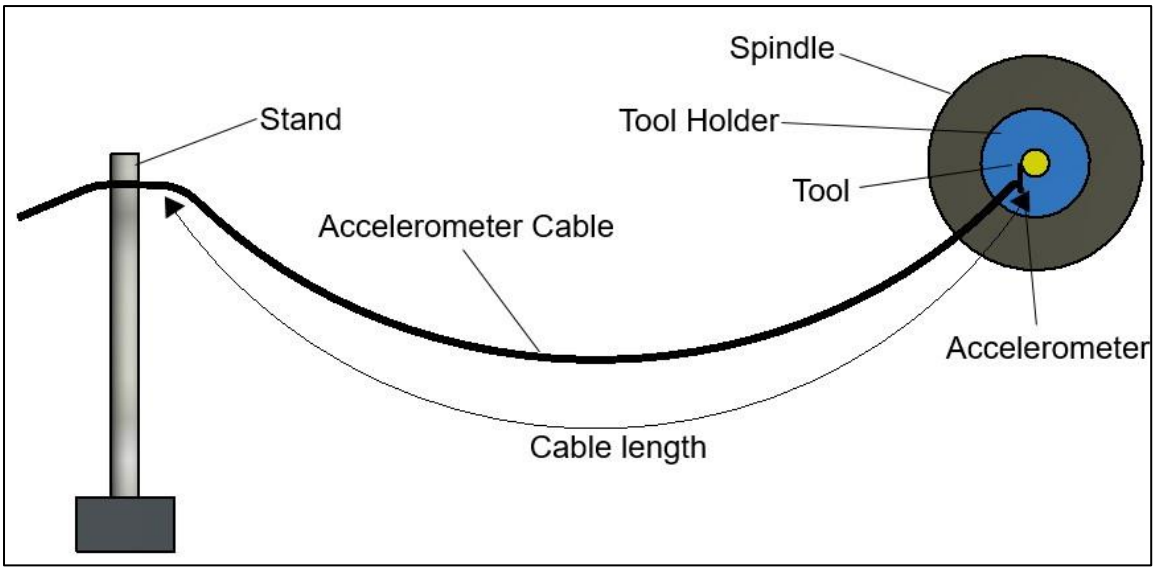

FIGURE 6.5.1. Schematic representation of 6.35 mm diameter rod setup with varying catenary cable lengths [47].

6.6. Case 5: Thin ribs with clamped-clamped-clamped-free boundary condition

Along with the 12.7 mm and 6.35 mm diameter rods, experiments were also carried out on two thin metal ribs with clamped-clamped-clamped-free boundary conditions. Two thin ribs made of 6061-T6 aluminum were used. Impact testing was carried out using the same miniature modal hammer and the vibration response was measured at the center of

the unsupported edge using the small accelerometer and the laser vibrometer. The ribs were clamped on the sides and the bottom edge was fixed to the workbench using cyanoacrylate as shown in figure 6.6.1.

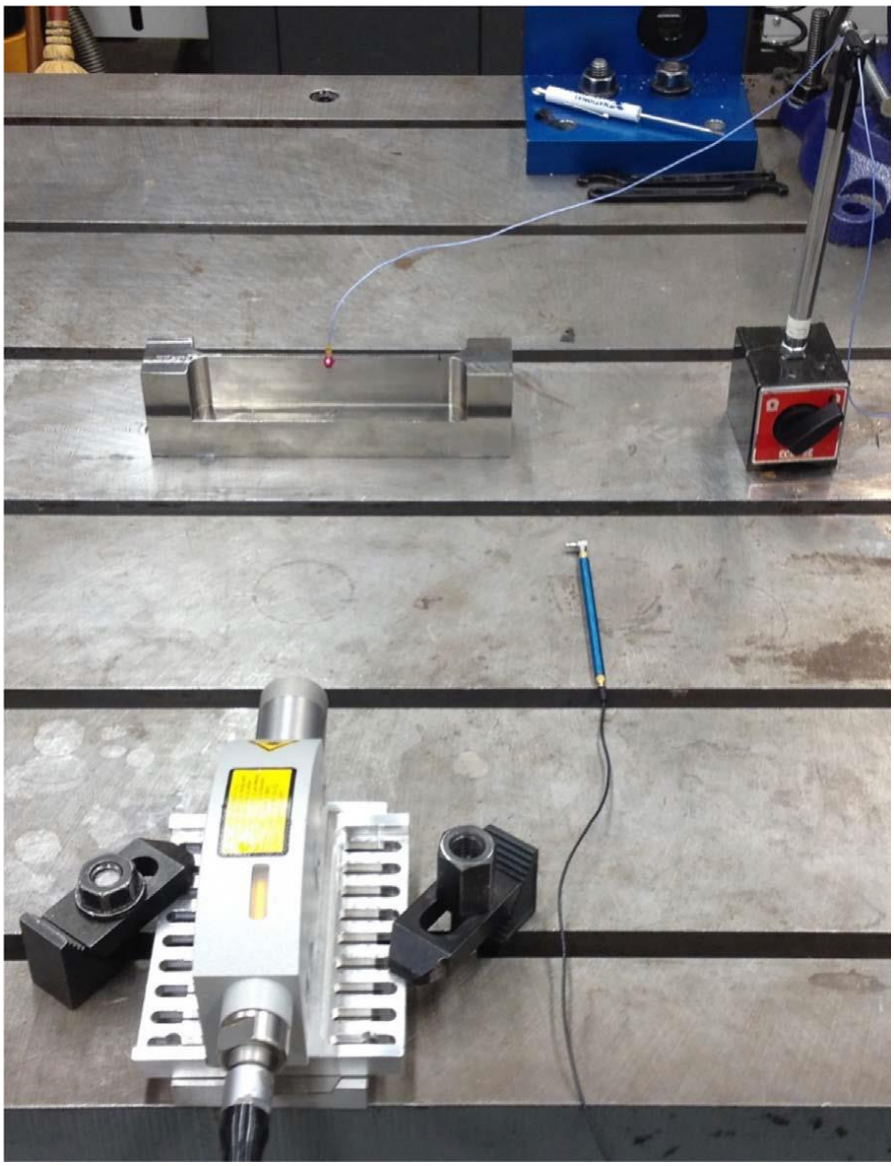

FIGURE 6.6.1. Setup for thin rib measurements [47].

CHAPTER 7: RESULTS AND DISCUSSION

The vibration responses of the 12.7 mm and 6.35 mm diameter steel rods were measured by impact testing using both accelerometers and a laser vibrometer. The accelerometer and the cable were removed from the rods along with the modal wax and their total mass was measured after every experiment. The accelerometer-cable FRF was modelled using Eq 6.3 (no damping) or Eq 6.4 (with damping). FRF data form the accelerometer and vibrometer measurements and modelling was processed in MATLAB®. Using IRCSA, the mass loading effect of the accelerometer was removed by subtracting the accelerometer-cable receptance from the rod receptance measured using the accelerometer. The IRCSA rod receptances were then compared with the rod receptances measured by laser vibrometer (no mass addition) to validate the effectiveness and accuracy of the mass loading compensation. The results for four cases are presented.

7.1. Case 1: 12.7 mm rod with clamped-free boundary condition

The measurements were recorded for the 12.7 mm diameter rod setup at overhang lengths of 102 mm, 111 mm, and 124 mm with both the accelerometers and vibrometer. For each overhang length and accelerometer combination, the FRF obtained by the IRCSA method was compared with the FRF obtained from the accelerometer and vibrometer measurements and these plots are shown in figures 7.1.1 through 7.1.6. It is observed in these plots that the natural frequency of the accelerometer FRF is lower than that of vibrometer FRF and the FRF obtained after correcting for mass loading matches closely with the vibrometer FRF. It can also be observed that the shift in the natural frequency is higher as the accelerometer mass increases. The effect of the cable on the amplitude of the

FRF is minimal. A summary of the 12.7 mm diameter rod measurement results for both accelerometers at three different overhang lengths is provided in Table 7.1.1. The average percent error in natural frequency was 1.02% for the medium accelerometer and 0.38% for the small accelerometer. The error reduced to 0.03% for the compensated results from all tests.

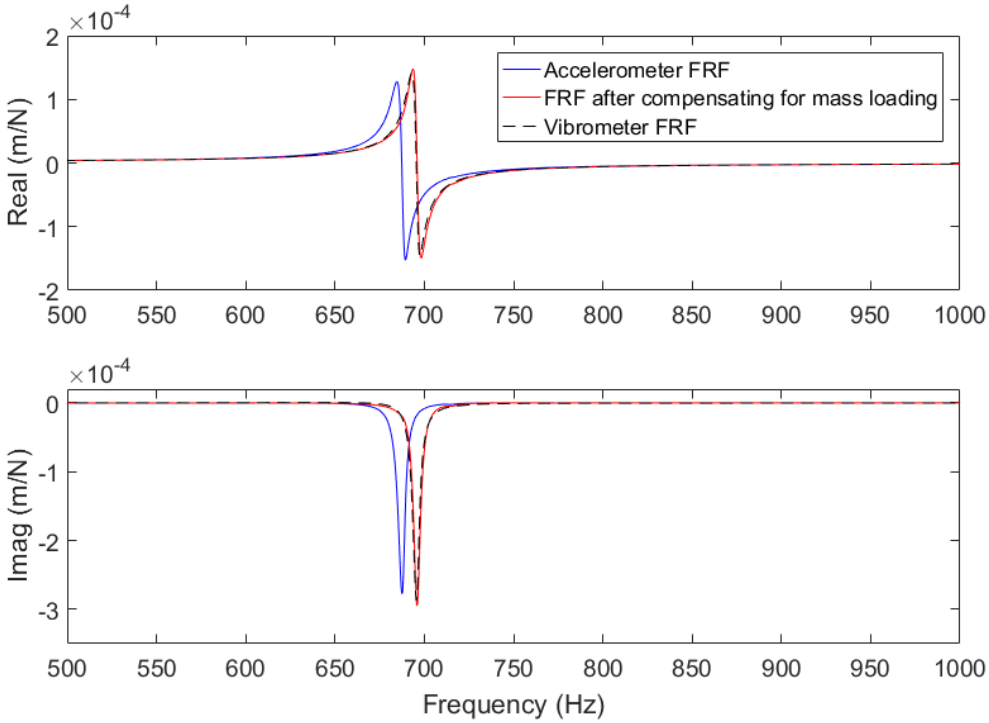

FIGURE 7.1.1. Results for 12.7 mm diameter rod with an overhang length of 102 mm using the medium accelerometer.

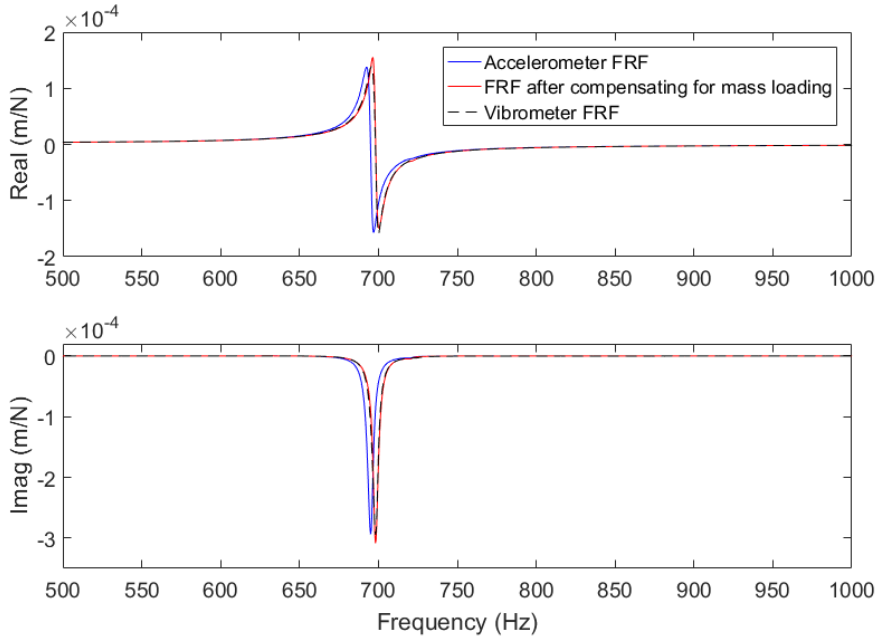

FIGURE 7.1.2. Results for 12.7 mm diameter rod with an overhang length of 102 mm using the small accelerometer.

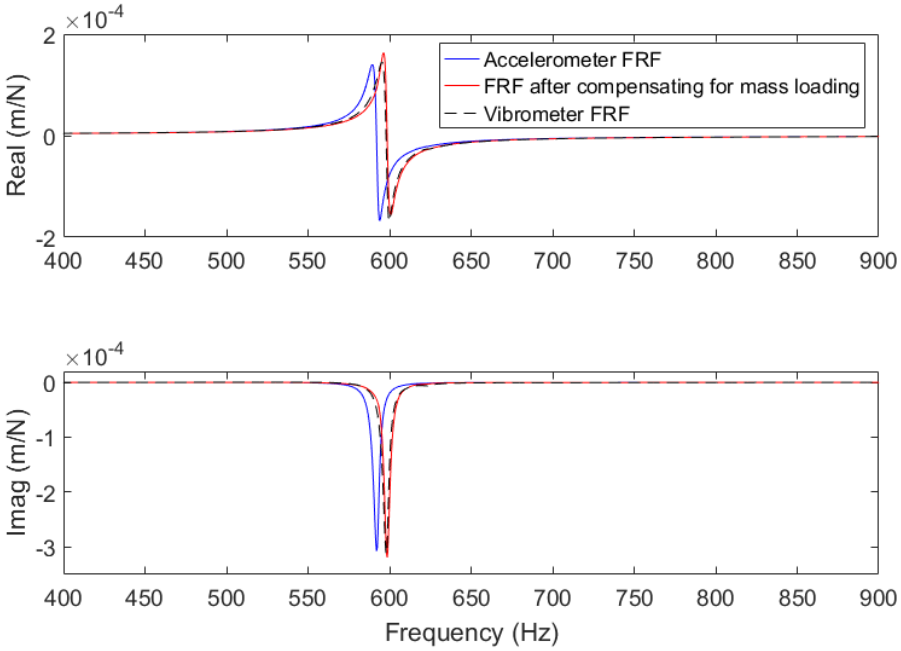

FIGURE 7.1.3. Results for 12.7 mm diameter rod with an overhang length of 111 mm using the medium accelerometer.

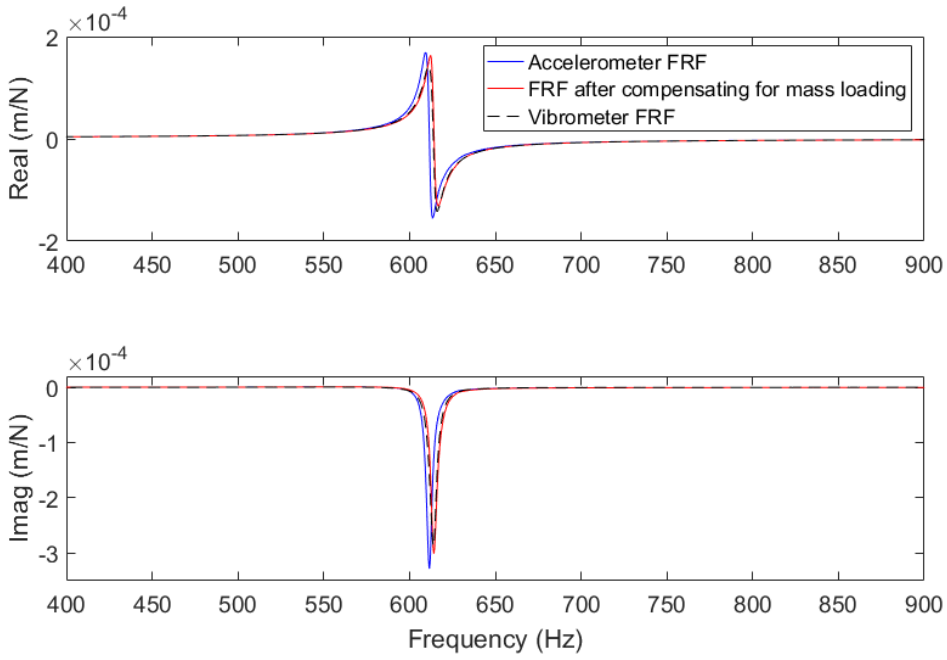

FIGURE 7.1.4. Results for 12.7 mm diameter rod with an overhang length of 111 mm using the small accelerometer.

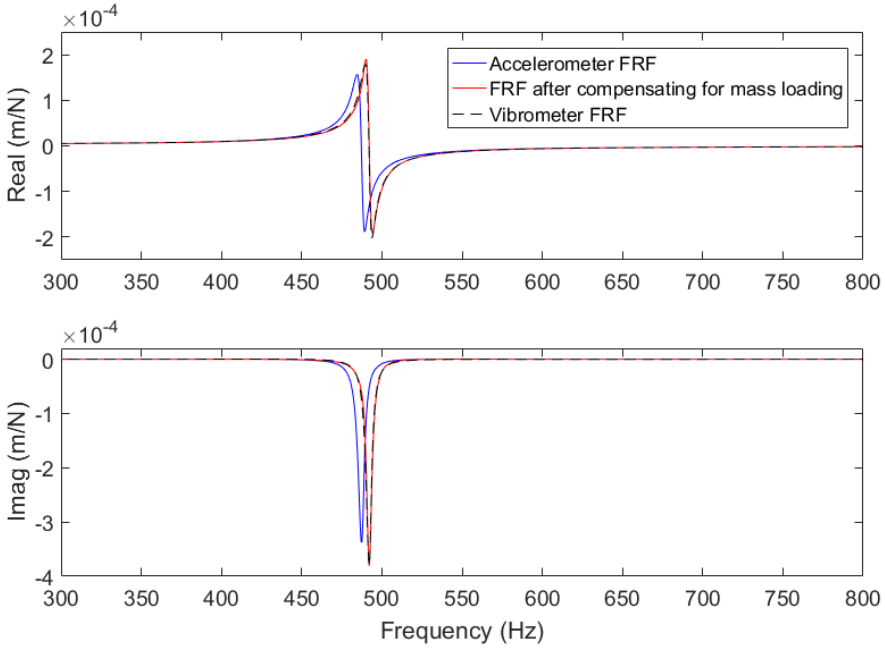

FIGURE 7.1.5. Results for 12.7 mm diameter rod with an overhang length of 124 mm using the medium accelerometer.

.

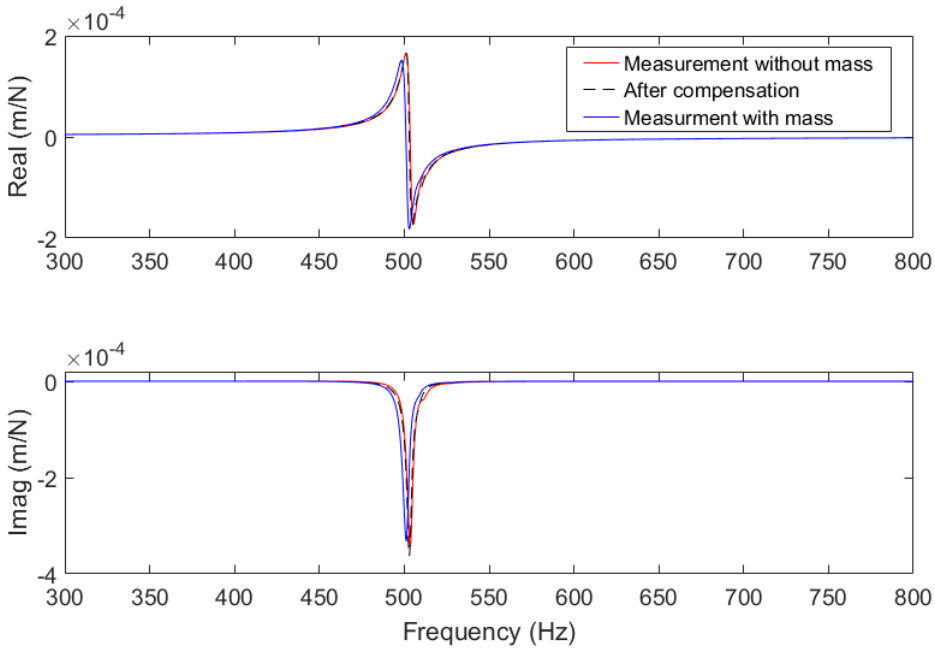

FIGURE 7.1.6. Results for 12.7 mm diameter rod with an overhang length of 124 mm using the small accelerometer.

TABLE 7.1.1: Results of mass loading correction for 12.7 mm diameter rod.

Overhang length (mm)	Vibrometer natural frequency (Hz)	Accelerometer natural frequency (Hz)	% error	Compensated natural frequency (Hz)	% error
Medium accelerometer (706 mg)					
102	695.4	687.4	1.10	695.8	-0.05
111	597.8	592	0.97	598.5	-0.11
124	492.1	487.1	1.01	492.1	0
Small accelerometer (275 mg)					
102	698.1	695	0.44	698.1	0
111	613.8	611.5	0.37	614.2	-0.06
124	503	501.3	0.33	502.8	0.03

7.2. Case 2: 6.35 mm rod with clamped-free boundary condition

Measurements were completed for the 6.35 mm diameter rod setup at overhang lengths of 79 mm and 89 mm with both accelerometers and the vibrometer. For each overhang length and accelerometer combination, the FRF obtained by the IRCSA method was compared with the FRF obtained from the accelerometer and vibrometer measurements. It was observed that when the accelerometer FRF was modelled using Eq 6.3 (no damping), the natural frequency of the accelerometer reading was compensated, but the amplitude did not match the vibrometer. This is shown in figure 7.2.1. So, Eq 6.4 was applied which considered the viscous damping effect of the cable. The value of viscous damping coefficient was varied until the amplitudes of the mass loading compensated FRF and the vibrometer FRF matched. These results are shown in figures 7.2.2 through 7.2.5. As it can be observed in these plots, the natural frequency of the accelerometer FRF is lower than that of vibrometer FRF and the FRF obtained after correcting for mass loading matches closely with the vibrometer FRF. It can also be observed that the shift in the natural frequency is higher as the accelerometer mass increases. The cable damping caused a significant change in the amplitude and the damping values used for correction are 1) c = 0.07 N-s/m for the small accelerometer; and 2) c=0.13 N-s/m and 0.15N-s/m for the medium accelerometer. A summary of the 6.35 mm diameter rod measurement results for both accelerometers at both overhang lengths is provided in Table 7.2.1. The average percent error in natural frequency was 5.8% for the medium accelerometer and 2.4% for the small accelerometer. The percent error reduced to 0.09% for the compensated results from all tests.

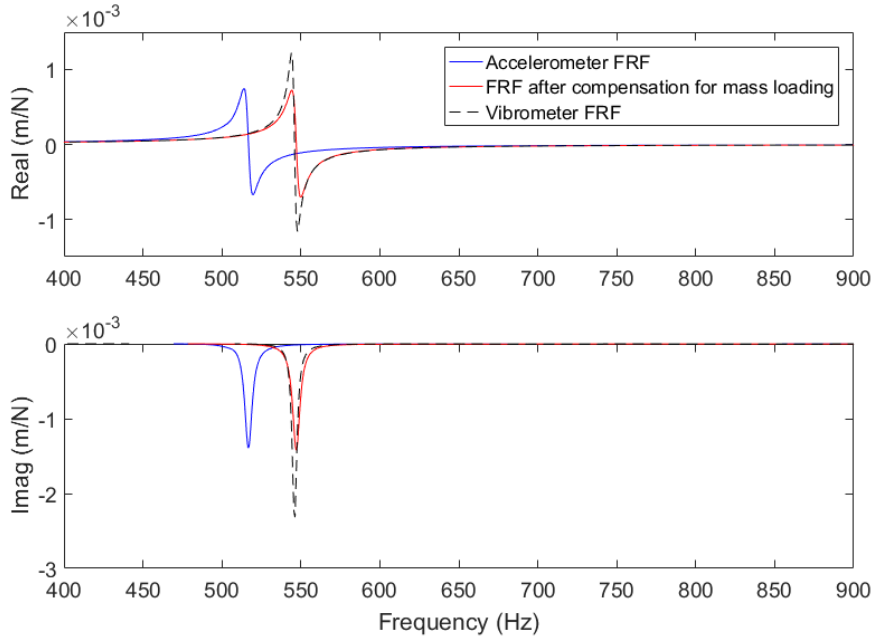

FIGURE 7.2.1. Results for 6.35 mm diameter rod with an overhang length of 89mm using the medium accelerometer without compensating for cable damping.

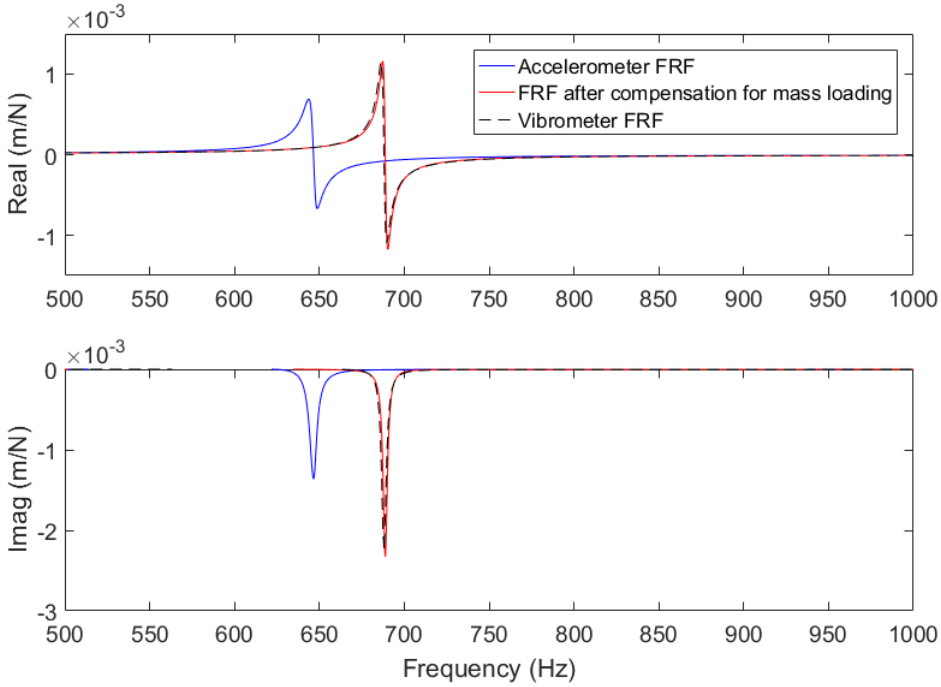

FIGURE 7.2.2. Results for 6.35 mm diameter rod with an overhang length of 79 mm using the medium accelerometer after compensating for cable damping.

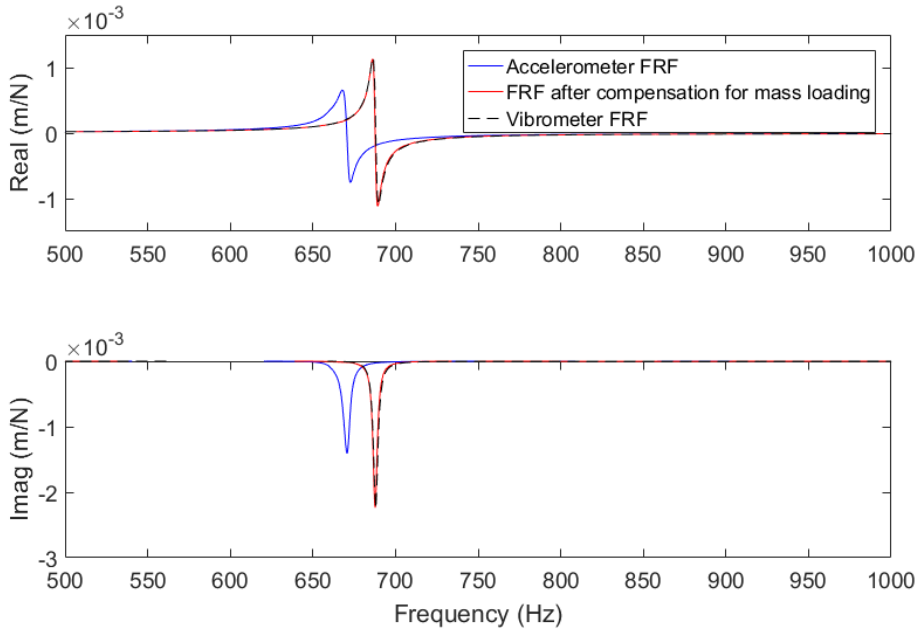

FIGURE 7.2.3. Results for 6.35 mm diameter rod with an overhang length of 79 mm using the small accelerometer after compensating for cable damping.

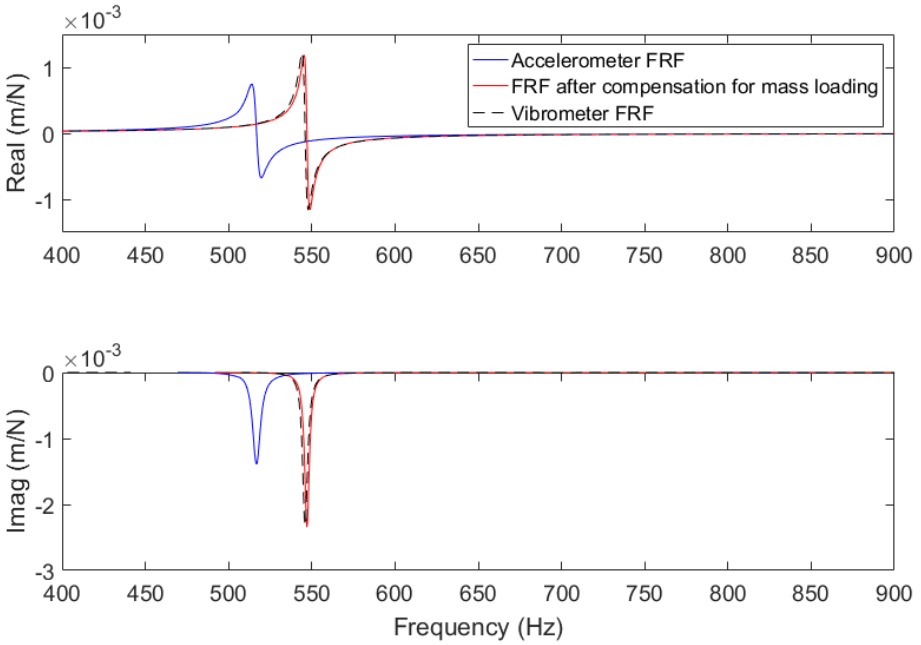

FIGURE 7.2.4. Results for 6.35 mm diameter rod with an overhang length of 89 mm using the medium accelerometer after compensating for cable damping.

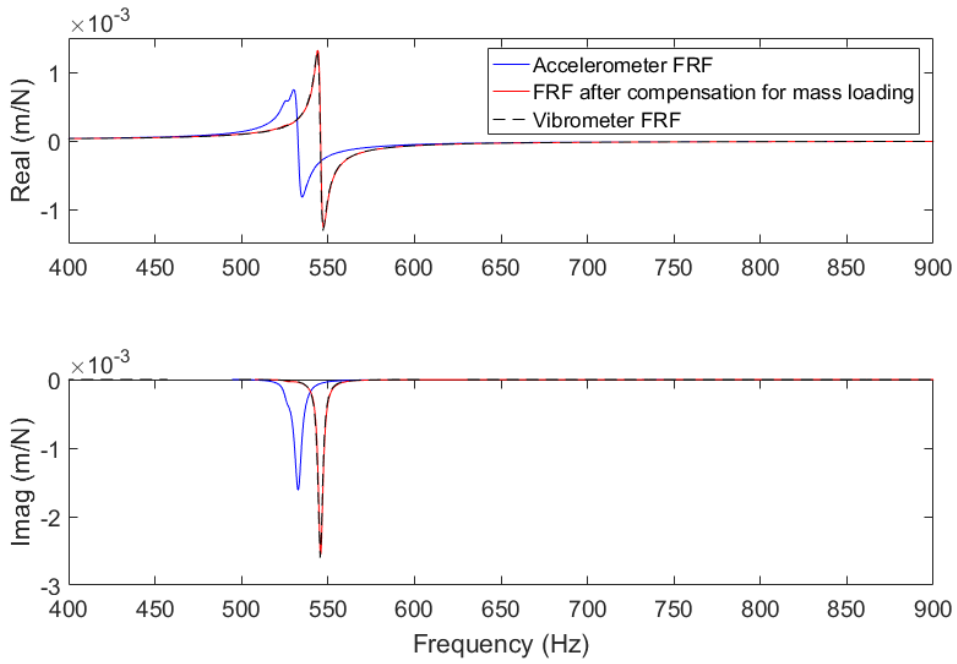

FIGURE 7.2.5. Results for 6.35 mm diameter rod with an overhang length of 89 mm using the small accelerometer after compensating for cable damping.

TABLE 7.2.1: Results of mass loading compensation for 6.35 mm diameter rod

Overhang length (mm)	Vibrometer natural frequency (Hz)	Accelerometer natural frequency (Hz)	% error	Compensated natural frequency (Hz)	% error
Medium accelerometer (680 mg)					
79	688.2	646	5.5	688.9	-0.10
89	546.3	516	6.1	547	-0.12
Small accelerometer (275 mg)					
79	687.8	671	2.4	688.2	-0.06
89	545.5	532.16	2.4	545.9	-0.07

7.3. Case 3: 6.35 mm rod with clamped-free boundary condition without accelerometer cable

To investigate the viscous cable damping effect on the accelerometer results, impact tests were performed on the 6.35 mm diameter rod for two overhang lengths of 79 mm and 89 mm with just the accelerometer attached at the free end (no cable). Impact tests

were also performed on the rod without any accelerometer attached to it. The vibration responses of the rod in both the cases were recorded using the laser vibrometer. The vibrometer readings were compared with each other and with the accelerometer readings from case 2 to verify the cable damping effect. These results are shown in figures 7.3.1 through 7.3.4. It can be observed that the shift in the natural frequency was caused by the accelerometer mass and the significant change in the amplitude of the FRF was caused by energy dissipation from cable motion.

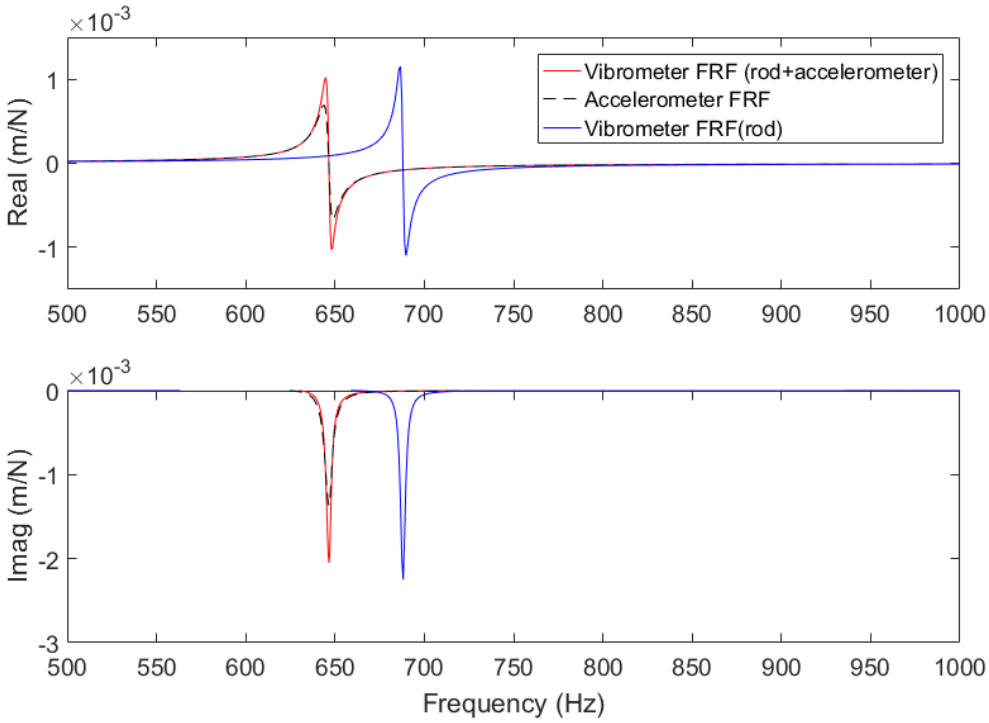

FIGURE 7.3.1. Results for 6.35 mm diameter rod with an overhang length of 79 mm using the medium accelerometer.

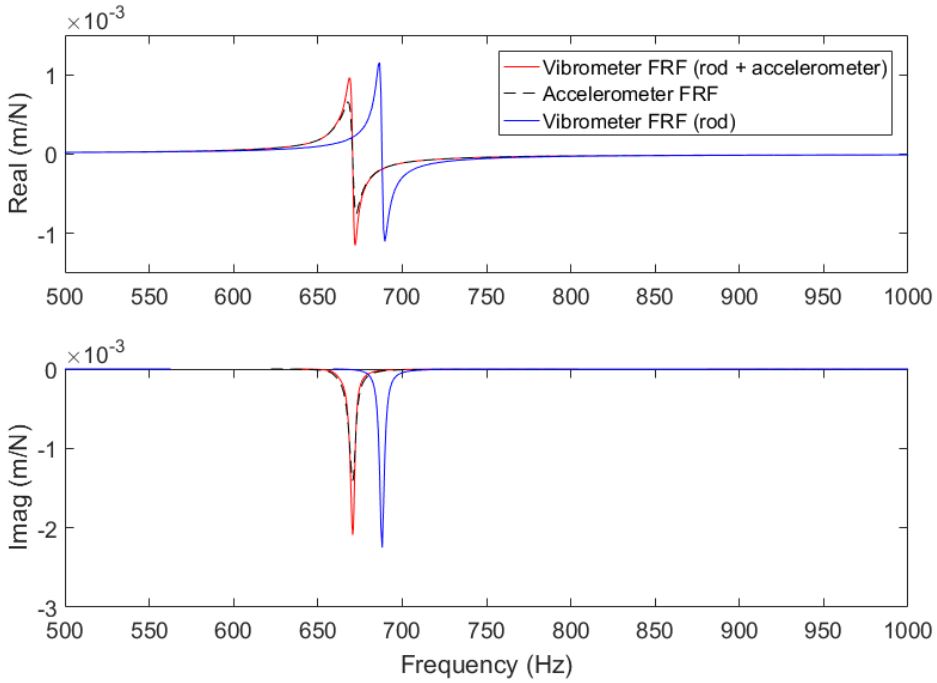

FIGURE 7.3.2. Results for 6.35 mm diameter rod with an overhang length of 79mm using the small accelerometer.

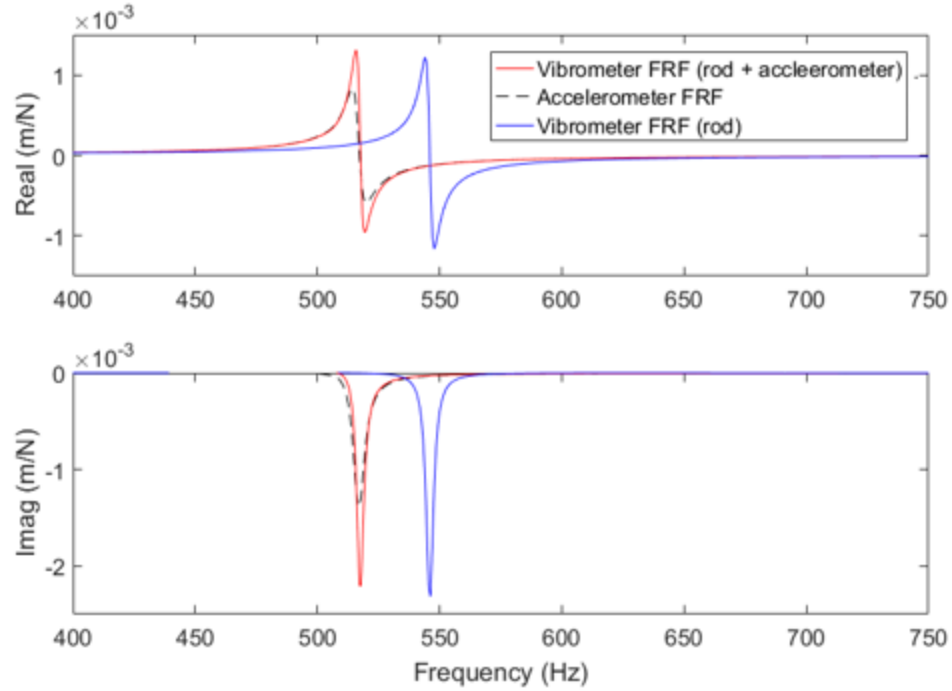

FIGURE 7.3.3. Results for 6.35 mm diameter rod with an overhang length of 89mm using the medium accelerometer.

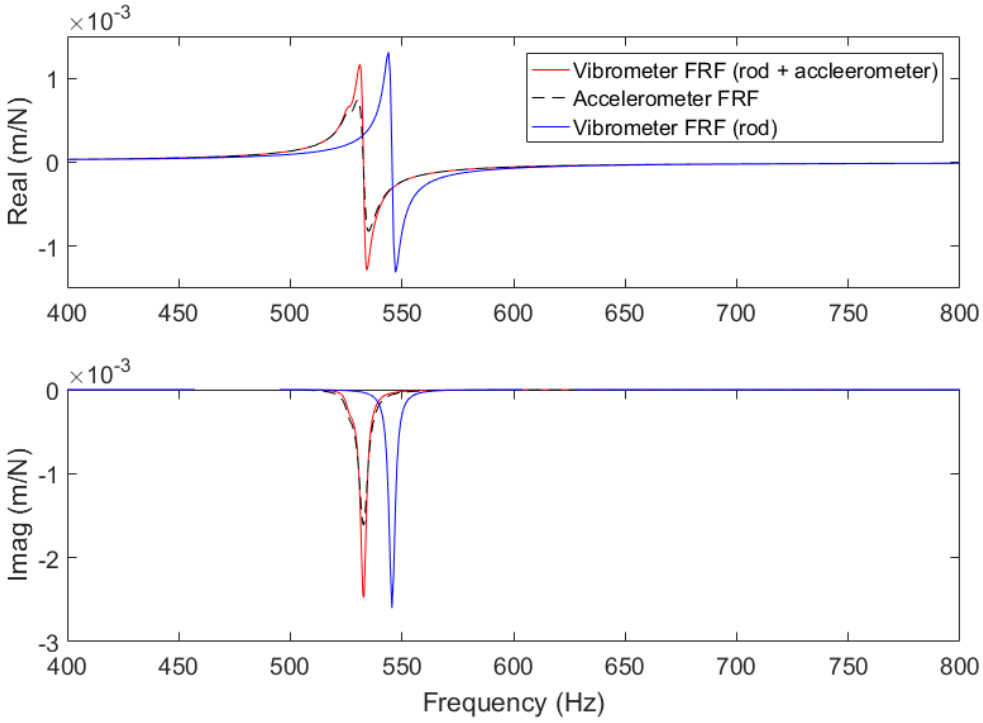

FIGURE 7.3.4. Results for 6.35 mm diameter rod with an overhang length of 89mm using the small accelerometer.

7.4. Case 4: 6.35 mm rod with clamped clamped-free boundary condition and varying accelerometer cable length

To understand the effect of cable length on the amount of damping and the corresponding effect on the accelerometer-based FRFs, tests were performed by varying the catenary length of the cable for a medium accelerometer and a large accelerometer attached to the free end of the 6.35 mm diameter rod. Three sets of measurements, {sets 1, 2, and 3}, were completed for each accelerometer. The cable was wound and left overnight between the sets. A fourth set of measurements, {set 4}, were recorded right after unwinding the cable to check if the cable hysteresis affected the measured FRFs. The catenary lengths of the cable were 304 mm, 608 mm, and 912 mm. As it was observed in

case 2, cable damping affected the amplitude of the FRF, so the magnitude of the FRFs was considered for this comparison. The results are shown in figures 7.4.1 through 7.4.10.

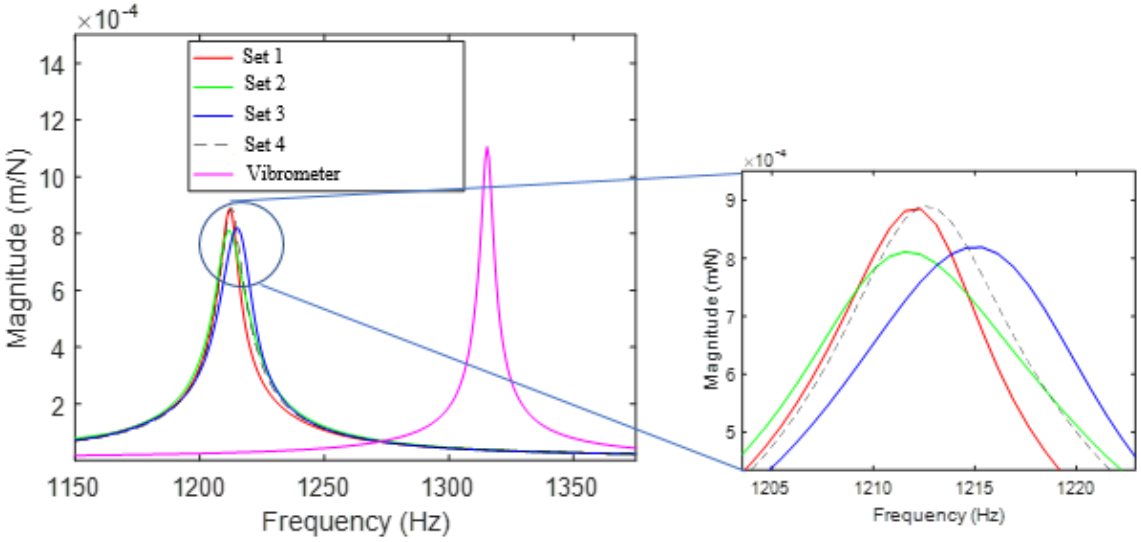

FIGURE 7.4.1. Results for 6.35 mm rod for an overhang length of 55 mm with medium accelerometer and catenary cable length of 304 mm.

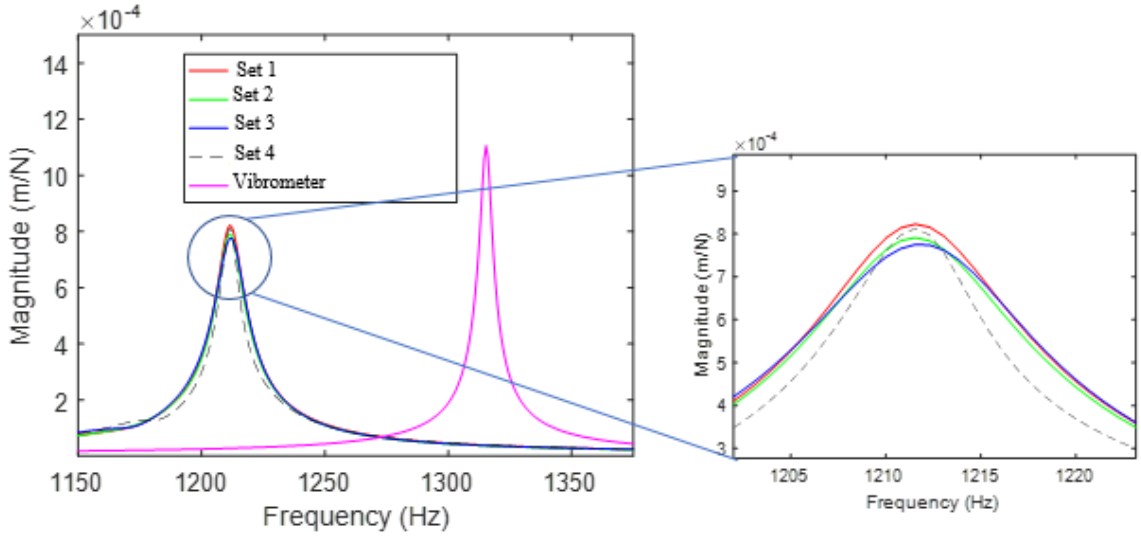

FIGURE 7.4.2. Results for 6.35 mm rod for an overhang length of 55 mm with medium accelerometer and catenary cable length of 608 mm.

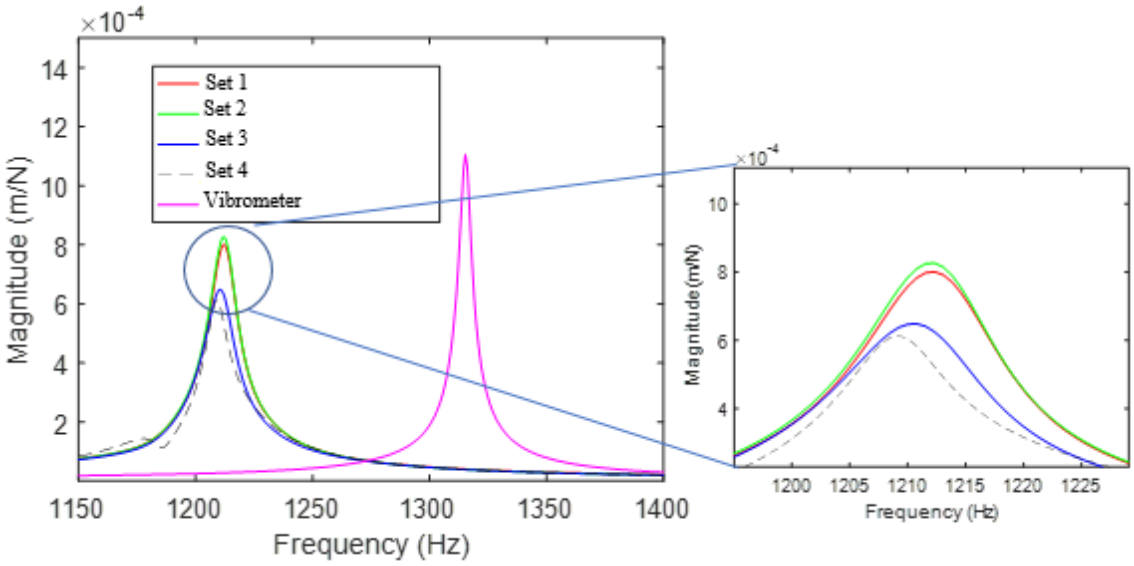

FIGURE 7.4.3. Results for 6.35 mm rod for an overhang length of 55 mm with medium accelerometer and catenary cable length of 912 mm.

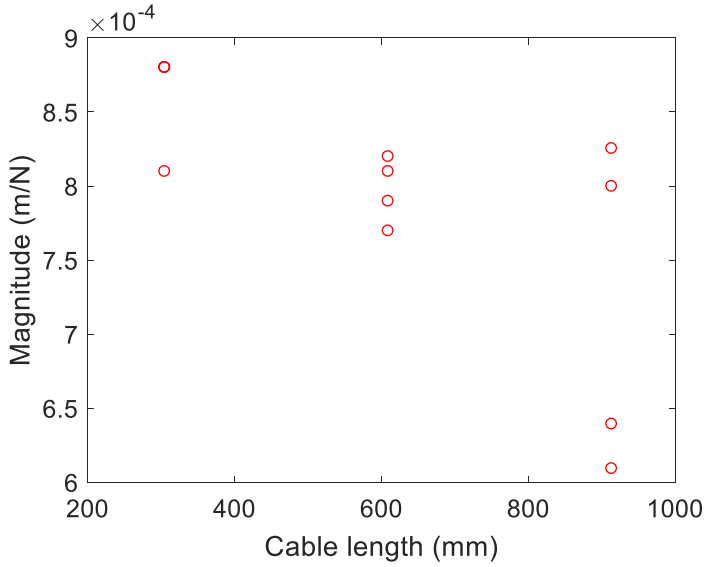

FIGURE 7.4.4. Cable length vs. FRF magnitude for the medium accelerometer attached at the free end of the 6.35 mm diameter rod with a 55-mm overhang length.

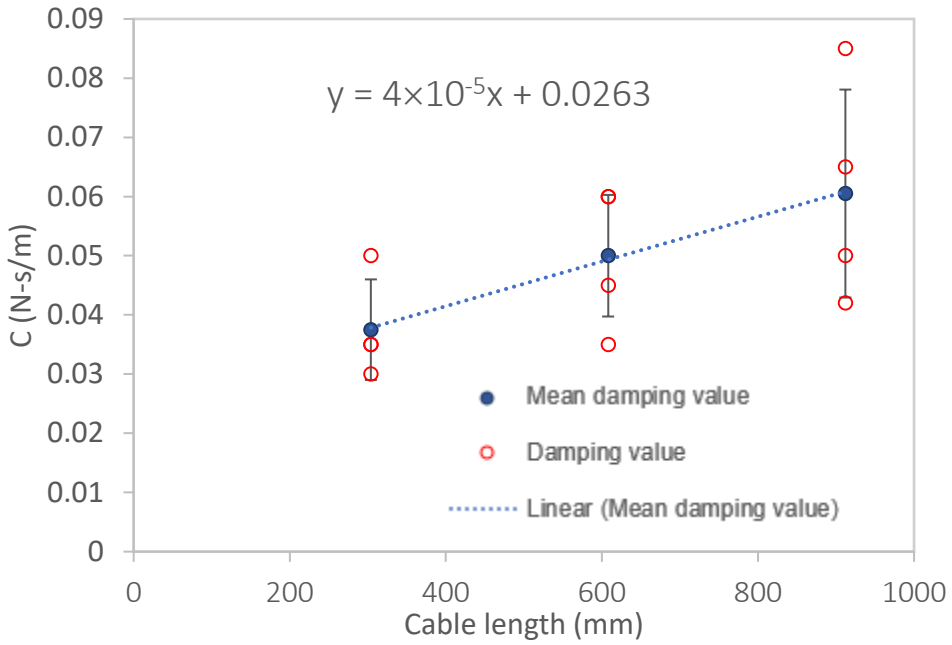

FIGURE 7.4.5. Plot of viscous damping coefficients used for mass loading correction vs. catenary cable length for medium accelerometer attached to the free end of the 6.35 mm diameter rod with 55 mm overhang length.

TABLE 7.4.1: Results for 6.35 mm rod for an overhang length of 55 mm with medium accelerometer and varying catenary cable length.

Cable length (mm)		Magnitude*10^{-4} (m/N)	c (N-s/m)
304	Set 1	8.8	0.035
	Set 2	8.1	0.030
	Set 3	8.8	0.050
	Set 4	8.8	0.035
608	Set 1	8.2	0.035
	Set 2	7.9	0.045
	Set 3	7.7	0.060
	Set 4	8.1	0.060
912	Set 1	8.0	0.065
	Set 2	8.3	0.042
	Set 3	6.4	0.085
	Set 4	6.1	0.050
Mean		8	0.049
Maximum difference		2.7	0.055
Standard deviation		0.83	0.015

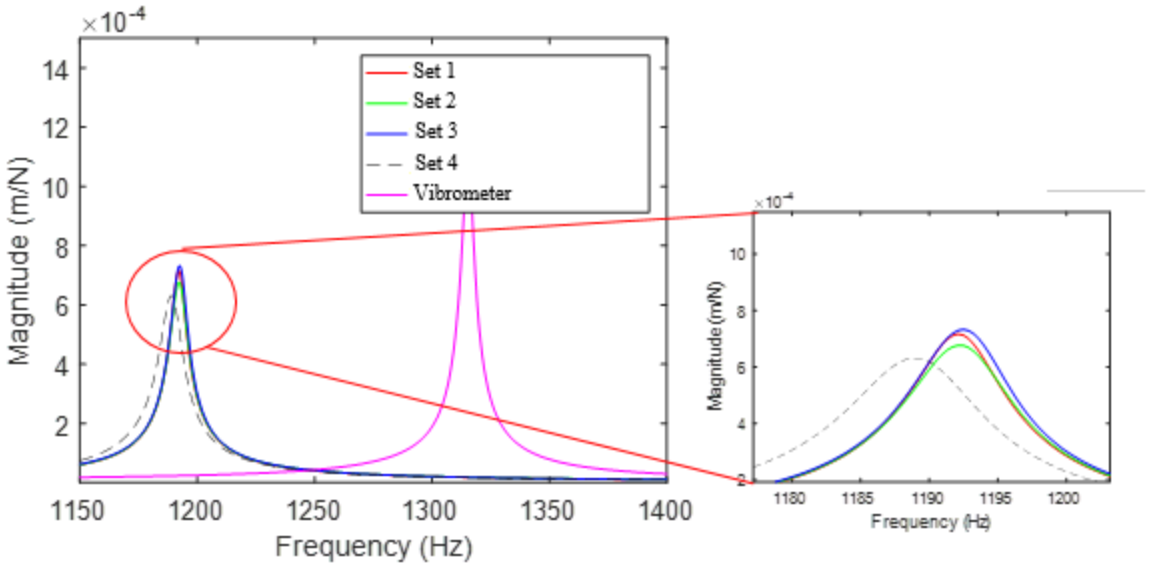

FIGURE 7.4.6. Results for 6.35 mm rod for an overhang length of 55 mm with large accelerometer and catenary cable length of 304 mm.

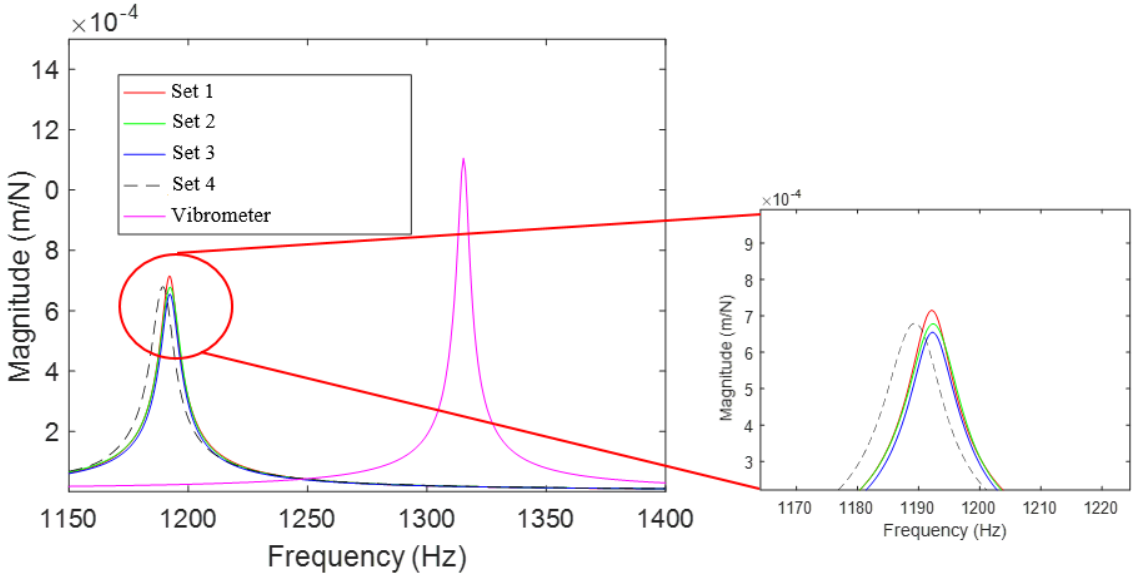

FIGURE 7.4.7. Results for 6.35 mm rod for an overhang length of 55 mm with large accelerometer and catenary cable length of 608 mm.

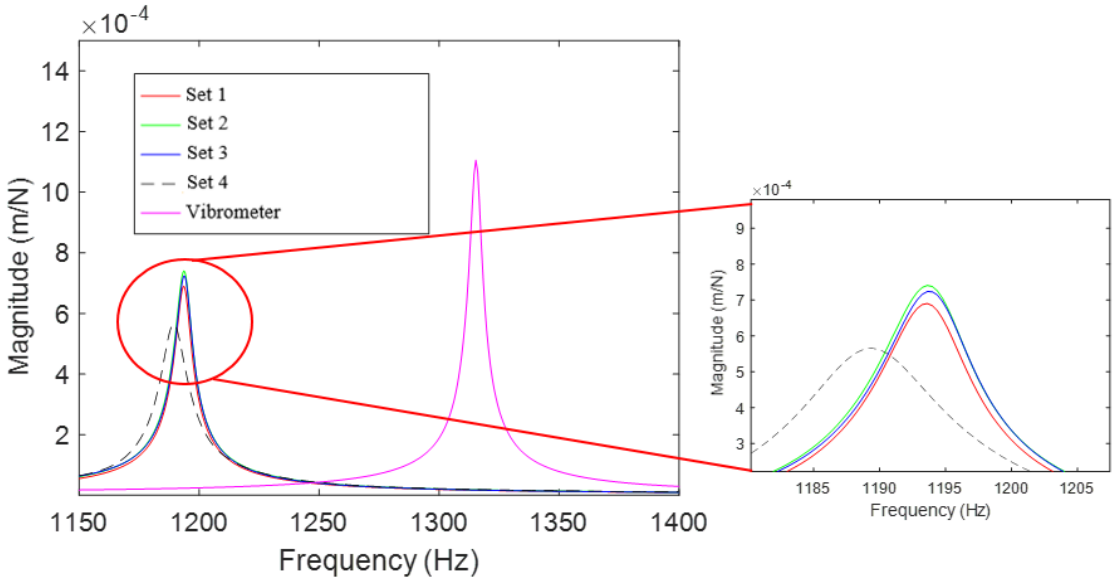

FIGURE 7.4.8. Results for 6.35 mm rod for an overhang length of 55 mm with large accelerometer and catenary cable length of 912 mm.

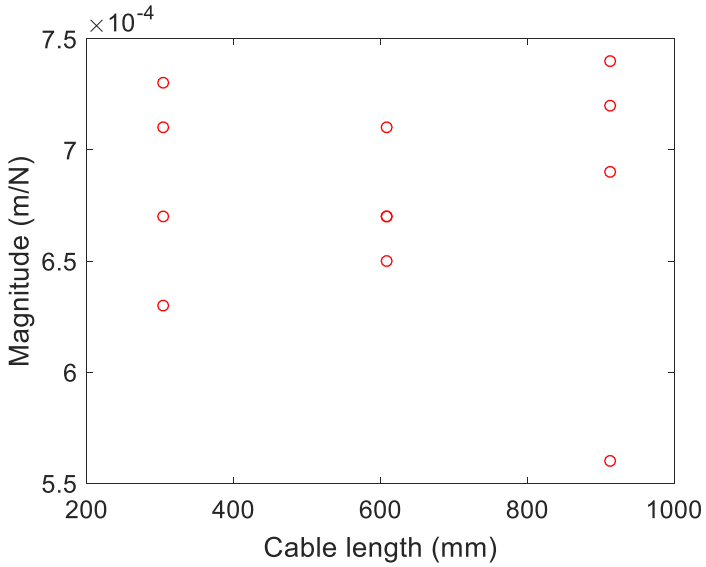

FIGURE 7.4.9. Cable length vs. magnitude of the accelerometer FRF for large accelerometer attached to the free end of the 6.35 mm diameter rod with 55 mm overhang length.

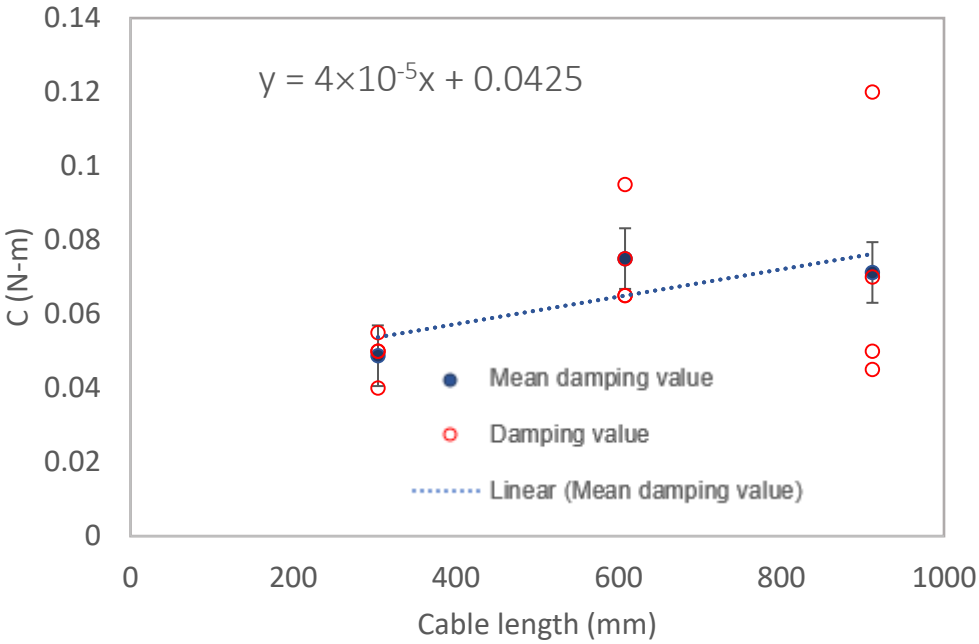

FIGURE 7.4.10. Plot of viscous damping coefficients used for mass loading compensation vs. catenary cable length for large accelerometer attached to the free end of the 6.35 mm diameter rod with 55 mm overhang length.

TABLE 7.4.2: Results for 6.35 mm rod for an overhang length of 55 mm with large accelerometer and varying catenary cable length.

Cable length (mm)		Magnitude*10^{-4} (m/N)	c (N-s/m)
304	Set 1	7.1	0.050
	Set 2	6.7	0.050
	Set 3	7.3	0.040
	Set 4	6.3	0.055
608	Set 1	7.1	0.065
	Set 2	6.7	0.065
	Set 3	6.5	0.075
	Set 4	6.7	0.095
912	Set 1	6.9	0.070
	Set 2	7.4	0.045
	Set 3	7.2	0.050
	Set 4	5.6	0.120
Mean		7	0.065
Maximum difference		1.8	0.080
Standard deviation		0.48	0.023

For constant conditions, identical results could not be obtained for the same cable catenary across the four data sets as observed in figures 7.4.1 to 7.4.3 and 7.4.6 to 7.4.8. However, the range of variation is reasonable.

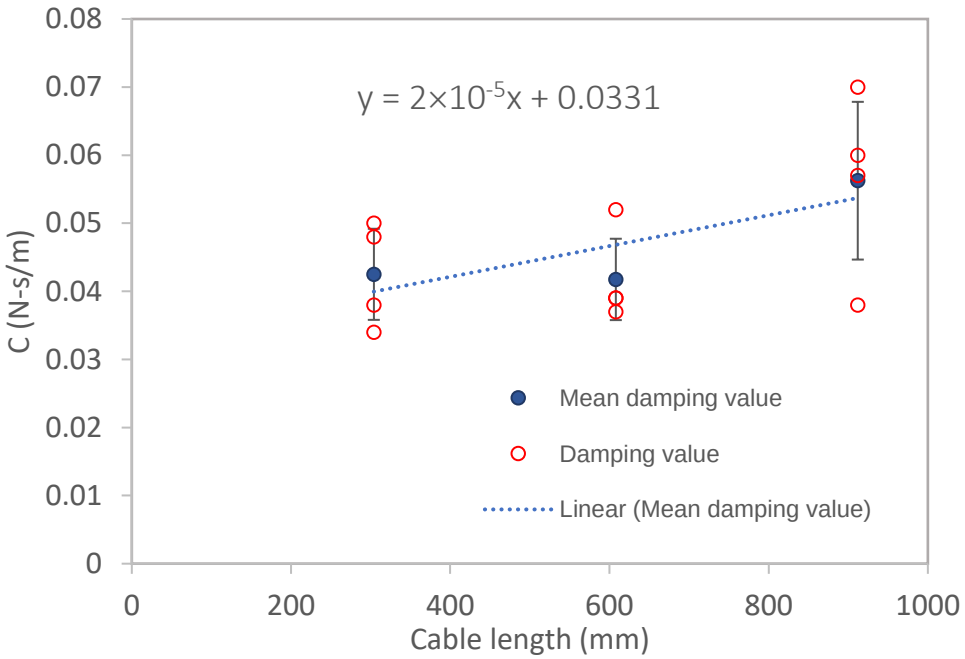

FIGURE 7.4.11. Plot of viscous damping coefficients used for mass loading compensation vs. catenary cable length for the medium accelerometer attached to the free end of the 6.35 mm diameter rod with 65 mm overhang length.

TABLE 7.4.3: Results for 6.35 mm rod for an overhang length of 65 mm with medium accelerometer and varying catenary cable length.

Cable length (mm)		Magnitude*10^{-4} (m/N)	c (N-s/m)
304	Set 1	9.80	0.038
	Set 2	9.60	0.050
	Set 3	9.08	0.048
	Set 4	9.99	0.034
608	Set 1	9.90	0.039
	Set 2	10.10	0.039
	Set 3	10.70	0.037
	Set 4	9.77	0.052
912	Set 1	9.60	0.060
	Set 2	9.50	0.057
	Set 3	10.30	0.038
	Set 4	8.70	0.070
Mean		10.0	0.046
Maximum difference		2.0	0.036
Standard deviation		0.51	0.011

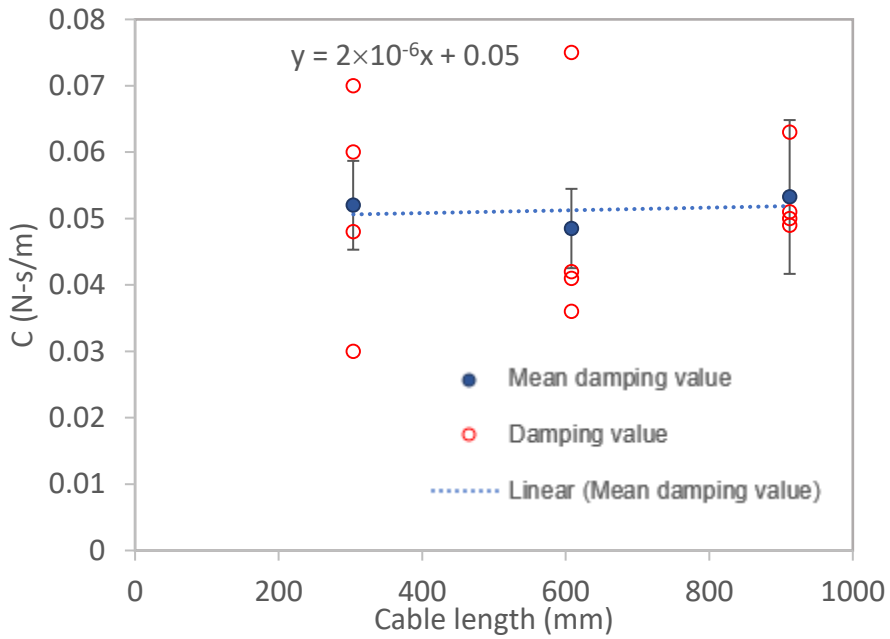

FIGURE 7.4.12. Plot of viscous damping coefficients used for mass loading compensation vs. catenary cable length for large accelerometer attached to the free end of the 6.35 mm diameter rod with 65 mm overhang length.

TABLE 7.4.4: Results for 6.35 mm rod for an overhang length of 65 mm with large accelerometer and varying catenary cable length.

Cable length (mm)		Magnitude*10^{-4} (m/N)	c (N-s/m)
304	Set 1	10.52	0.03
	Set 2	9.20	0.06
	Set 3	9.16	0.048
	Set 4	8.20	0.07
608	Set 1	9.43	0.041
	Set 2	9.45	0.036
	Set 3	8.70	0.075
	Set 4	8.80	0.042
912	Set 1	8.90	0.049
	Set 2	9.08	0.051
	Set 3	9.20	0.05
	Set 4	8.60	0.063
Mean		9	0.051
Maximum difference		2.32	0.045
Standard deviation		0.55	0.012

The slope of the linear regression fit for mean damping values, as seen in figures 7.4.5 and 7.4.10, was the same for the rod with a 55 mm overhang length, but this was not observed for the rod with a 65 mm overhang length as shown in figures 7.4.11 and 7.4.12. Therefore, a conclusive relationship between the catenary length of the cable and the resultant damping coefficient could not be established. Also, it was observed that the mean damping value seemed to increase with the stiffness of the rod, 0.46 to 0.49 for the medium accelerometer and 0.51 to 0.65 for the large accelerometer.

7.5. Case 5: Thin ribs with clamped-clamped-clamped-free boundary condition.

To test the accuracy of this mass compensation technique for structures with different boundary conditions and geometries, measurements were recorded for 150 x 20 x 2 mm and 100 x 20 x 3 mm aluminum ribs, which were designated as rib 1 and rib 2, respectively, with the medium accelerometer and laser vibrometer. The accelerometer-

cable FRF was modelled using Eq 6.4 to account for the cable damping. For each rib, the FRF obtained by the IRCSA method was compared with the FRF obtained from the accelerometer and vibrometer measurements. Similar to the measurements of the clamped-free rods, a shift in the natural frequency and decrease in magnitude was observed for the accelerometer FRFs as seen in figures 7.5.1 and 7.5.2.

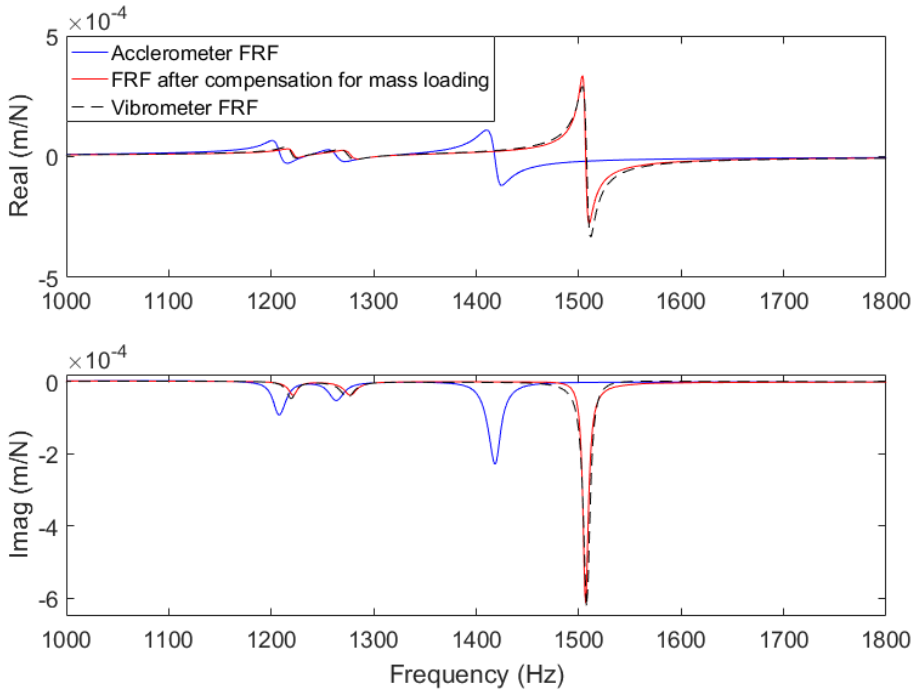

FIGURE 7.5.1. Results for 150 x 20 x 2 mm aluminum rib (rib 1) with medium accelerometer.

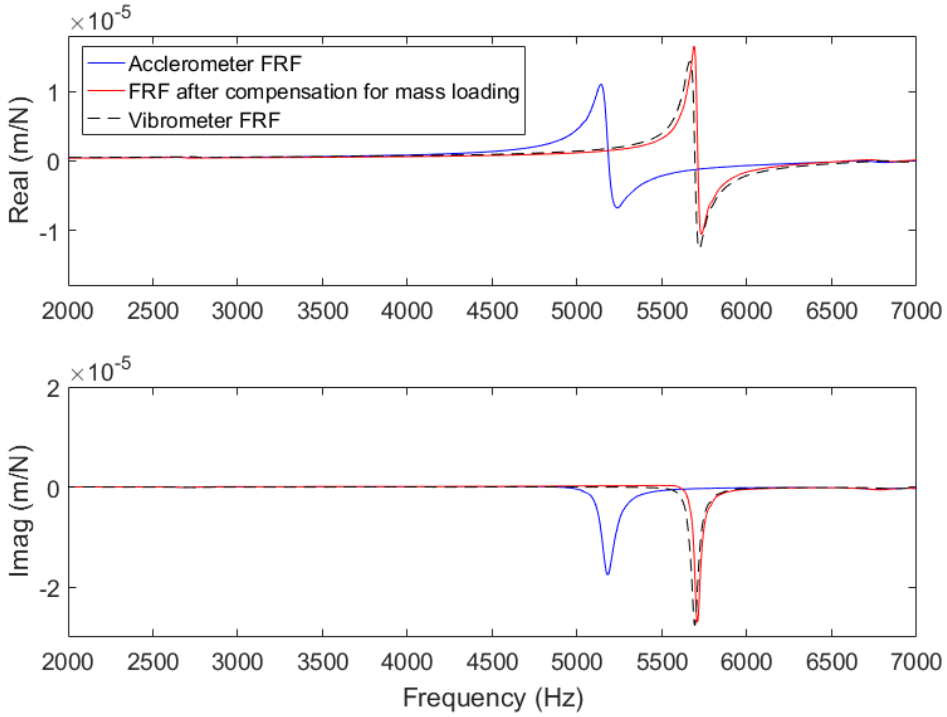

FIGURE 7.5.2. Results for 100 x 20 x 3 mm aluminum rib (rib 2) with medium accelerometer .

.

.

For rib 1 the percent error in natural frequency was reduced from 5.97% to 0.07%. For rib 2 the percent error in natural frequency was reduced from 9.08% to -0.26%. The damping effect of the cable may scale with the structure stiffness as it was observed that for the same mass of accelerometer and length of the cable, the damping valued used for the compensation for rib 1 and rib 2 were 0.18 and 0.92, respectively.

7.6. Effects of mass loading and cable damping compensation on stability lobe diagrams.

Stability lobe diagrams were generated for a two-tooth 6.35 mm diameter tool (55 mm overhang length) performing a 25% up milling operation in an aluminium alloy (750 N/mm^2 specific cutting force and 68 deg force angle). The tool FRF was approximated using measured data from the 6.35 mm diameter steel rod with an overhang length of 55 mm. Stability lobe diagrams for four cases are presented in figure 7.6.1: accelerometer, vibrometer, accelerometer with mass compensation only, and accelerometer with both mass and damping compensation. As expected, the uncompensated accelerometer and vibrometer stability lobes differ. The stability lobe diagram generated using both mass and damping compensation closely agrees with the vibrometer diagram, however. The stability lobe diagram generated using only mass compensation matches in spindle speed (Ω), but overestimates the allowable axial depth of cut (b_{lim}) slightly.

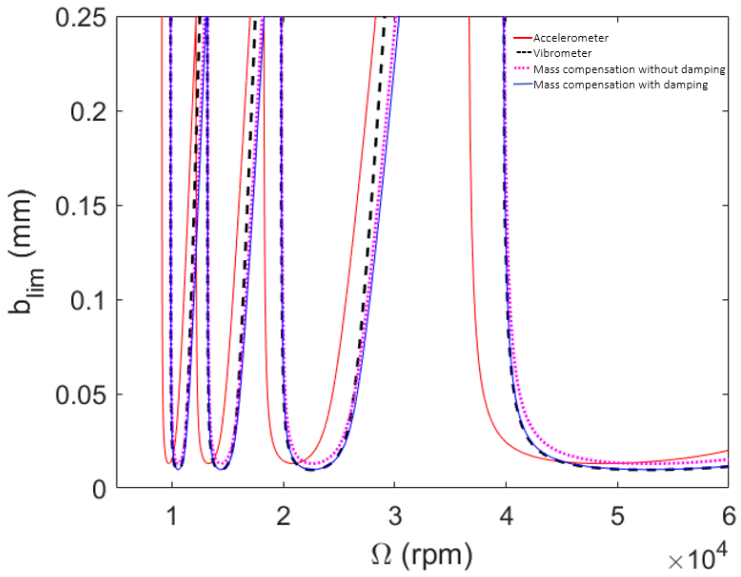

FIGURE 7.6.1. Stability lobe diagrams for end milling with 25% radial immersion up milling generated using different FRFs.

The variation in the stability limit with the compensation damping value was also explored. Based on the prior results with the hanging cable repetitions, a mean (c) and standard deviation (σ_c) was identified for the 6.35 mm diameter rod with a 55 mm overhang damping compensation value. Stability lobe diagrams are displayed in figure 7.6.2 for three cases: mean c, mean c plus one standard deviation, and mean c minus one standard deviation compensation, where the mean c value was 0.049 N-s/m and the standard deviation was 0.015 N-s/m. The damping variation had only a slight impact on the limiting axial depth of cut.

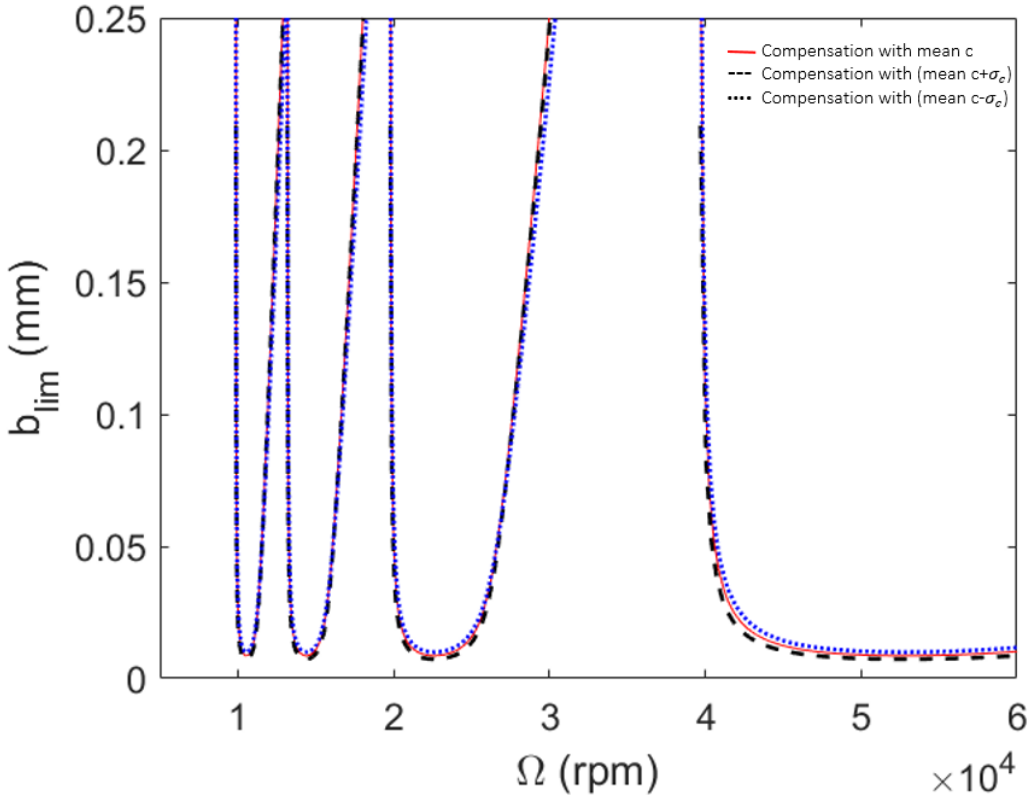

FIGURE 7.6.2. Stability lobe diagrams for end milling with 25% radial immersion generated using FRFs corrected with different c values.

CHAPTER 8: SUMMARY AND CONCLUSION

In this work, inverse receptance coupling substructure analysis (IRCSA) was proposed to compensate for the mass loading and damping effect of the accelerometer and its cable on the FRF measurements of low mass structures. The motivation for this study was to enable more accurate FRF measurements with accelerometers, which are a popular due to the ease of setup and use. This would result in increased accuracy for stability lobe diagrams, which are used to select stable machining parameters. A brief introduction to FRFs and a literature review were presented first. This was followed a description of receptance coupling. FRF measurement techniques used in this study were then detailed along with possible errors.

Five different cases were studied to gain a better understanding of how the accelerometer mass loading and cable damping affect measurement accuracy for systems with different dynamics. The accuracy of the mass loading compensation was also evaluated. FRFs were measured using accelerometers and a vibrometer, which provided a non-contact measurement reference with no mass loading. A model of the accelerometer-cable FRF was decoupled from the measured FRF using IRCSA to compensate for the accelerometer mass loading and cable damping. The resultant IRCSA FRF was then compared to the vibrometer FRF to validated the compensation technique.

In the cases 1 and 2, two steel rods of 12.7 mm and 6.35 mm diameter with clamped-free boundary conditions were measured with the same accelerometer to study how the

same mass loading affects structures with different modal masses. Measurements were taken at different overhang lengths to vary both the modal stiffness and mass of the rods.

In case 3, measurements were completed using the accelerometer, but with no cable. The accelerometer was attached to the free end of the 6.35 mm diameter rod. This removed the cable damping effect and enable a comparison to test 1 and 2, which included the cable. For case 4, the cable was again included. The cable was supported by a metal stand and the catenary length of the cable was systematically varied between 304 mm, 608 mm, and 912 mm to study the effect of cable length on the amount of damping. Experiments were performed at two rod overhang lengths to compare the results. In case 5, impact tests were performed on two clamped-clamped-clamped-free aluminium ribs to verify the accuracy of the mass loading correction technique on structures with different geometry and boundary conditions. The modal stiffness was an order an order of magnitude different for the two ribs.

Results from all tests indicated that the accelerometer-cable mass affected the natural frequencies, while the damping had a significant effect on the magnitudes. As the mass of the accelerometer increased, the shift in the natural frequency also increased. In case 1, the length of the cable was too short to have a noticeable damping effect, so only the accelerometer-cable mass was considered and the compensated FRF matched with vibrometer measurement. In case 2, when the cable length was large enough to have a damping effect on the accelerometer-based FRF, the damping value had to be included in the accelerometer-cable FRF model. Using this model, the compensated FRFs matched the vibrometer FRFs when appropriate viscous damping coefficients were included in the accelerometer-cable model. Results from case 3 showed that the significant change in the

FRF magnitudes measured using accelerometers was caused by cable energy dissipation. The attempts to directly relate the cable length to the amount of damping with the results from case 4 were not successful. Although the average damping values (generally increased with cable length, the dispersion was large. To further investigate the relationship between the compensation damping value and the system dynamics, figures 8.1 and 8.2 display the variation in damping with modal stiffness, k, and natural frequency, f_n, respectively. In both cases, a linear relationship is observed. This result can potentially be used in future work to develop a predictive damping model for accelerometer cable damping compensation.

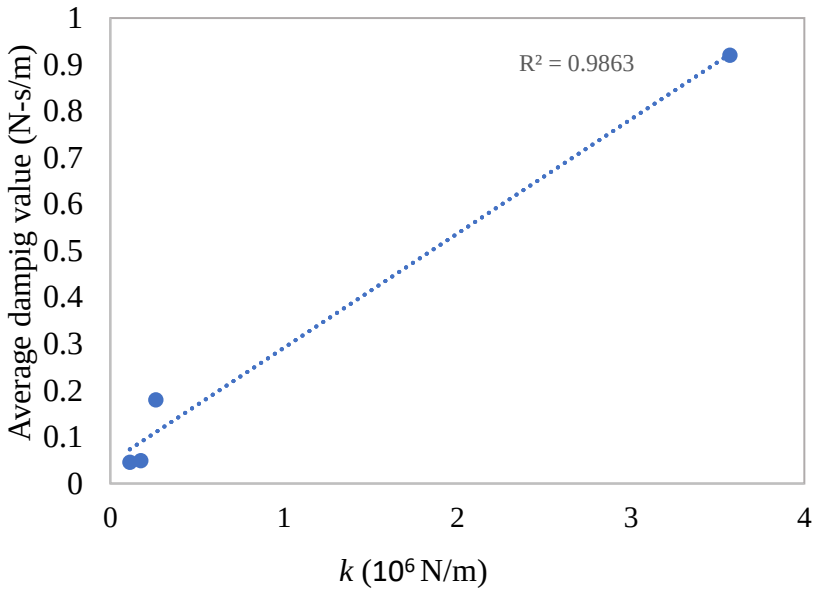

FIGURE 8.1. Modal stiffness vs average damping value.

TABLE 8.1: Modal stiffness vs. average damping values.

Structure	k (N/m)	Average c value (N-s/m)
6.35 mm rod – 65 mm overhang length	1.12×10^5	0.046
6.35 mm rod – 55 mm overhang length	1.75×10^5	0.049
Aluminum rib - 150 x 20 x 2 mm	2.62×10^5	0.18
Aluminum rib - 100 x 20 x 3 mm	35.7×10^5	0.92

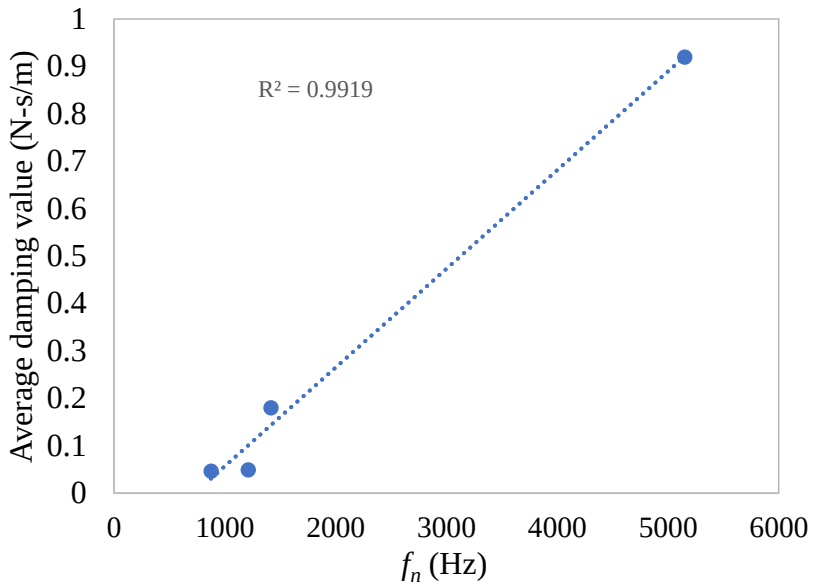

FIGURE 8.2. Frequency vs average damping value.

Table 8.2: Natural frequency vs. average damping values.

Structure	f_n (Hz)	Average c value (N-s/m)
6.35 mm rod – 65 mm overhang length	875	0.046
6.35 mm rod – 55 mm overhang length	1212	0.049
Aluminum rib - 150 x 20 x 2 mm	1415	0.18
Aluminum rib - 100 x 20 x 3 mm	5150	0.92

The mass loading compensation technique reduced the percent error between the vibrometer and compensated FRFs to the tenths of a percent level for both the clamped-free rods and the thin ribs with different boundary conditions and geometry. This was reflected in the stability lobe diagrams, where the diagram generated using the compensated accelerometer FRF matched very closely with that generated from the vibrometer FRF. This demonstrates that the IRCSA technique can be implemented to compensate for mass loading and damping effects of the accelerometer-cable for any dynamic structure.

REFERENCES

[1] Bishop R, Johnson D (1960) The mechanics of vibration. Cambridge University Press, Cambridge

[2] Schmitz TL, Davies MA, Kennedy MD. Tool Point Frequency Response Prediction for High-Speed Machining by RCSA. ASME. J. Manuf. Sci. Eng. 2001;123(4):700-707. doi:10.1115/1.1392994.

[3] Schmitz, Tony L., Michael Kennedy, and Matthew A. Davies. "Tool point frequency response prediction for high-speed machining by RCSA." Journal of Manufacturing Science and Engineering-Transactions of the ASME 123 (2001).

[4] Schmitz, Tony L., et al. "Improving high-speed machining material removal rates by rapid dynamic analysis." CIRP Annals-Manufacturing Technology50.1 (2001): 263-268.

[5] Duncan, G. Scott, M. F. Tummond, and Tony L. Schmitz. "An investigation of the dynamic absorber effect in high-speed machining." International Journal of Machine Tools and Manufacture 45.4 (2005): 497-507.

[6] Albertelli, Paolo, et al. "The effects of dynamic interaction between machine tool subsystems on cutting process stability." The International Journal of Advanced Manufacturing Technology 58.9 (2012): 923-932.

[7] Kivanc, E. B., and Erhan Budak. "Structural modeling of end mills for form error and stability analysis." International Journal of Machine Tools and Manufacture 44.11 (2004): 1151-1161.

[8] Movahhedy, Mohammad R., and Javad M. Gerami. "Prediction of spindle dynamics in milling by sub-structure coupling." International Journal of Machine Tools and Manufacture 46.3 (2006): 243-251.

[9] Park, S. S., and J. Chae. "Joint identification of modular tools using a novel receptance coupling method." The International Journal of Advanced Manufacturing Technology 35.11 (2008): 1251-1262.

[10] Park, Simon S., Yusuf Altintas, and Mohammad Movahhedy. "Receptance coupling for end mills." International Journal of Machine Tools and Manufacture 43.9 (2003): 889-896.

[11] Mancisidor, Iker, et al. "Receptance Coupling for Tool Point Dynamics Prediction." 17th CIRP International Conference on Modelling of Machining Operations. 2011.

[12] Özşahin, O., and Y. Altintas. "Prediction of frequency response function (FRF) of asymmetric tools from the analytical coupling of spindle and beam models of holder and tool." International Journal of Machine Tools and Manufacture 92 (2015): 31-40.

[13] Albertelli, P., M. Goletti, and M. Monno. "A new receptance coupling substructure analysis methodology to improve chatter free cutting conditions prediction." International Journal of Machine Tools and Manufacture 72 (2013): 16-24.

[14] Schmitz, Tony L. "Torsional and axial frequency response prediction by RCSA." Precision Engineering 34.2 (2010): 345-356.

[15] Duncan, G. Scott, and T. Schmitz. "An improved RCSA model for tool point frequency response prediction." Proceedings of the 23rd International Modal Analysis Conference. Vol. 30. 2005.

[16] Ertürk, A., H. N. Özgüven, and Erhan Budak. "Analytical modeling of spindle–tool dynamics on machine tools using Timoshenko beam model and receptance coupling for the prediction of tool point FRF." International Journal of Machine Tools and Manufacture 46.15 (2006): 1901-1912.

[17] Ahmadian, Hamid, and Mostafa Nourmohammadi. "Tool point dynamics prediction by a three-component model utilizing distributed joint interfaces." International Journal of Machine Tools and Manufacture 50.11 (2010): 998-1005.

[18] Namazi, Mehdi, et al. "Modeling and identification of tool holder–spindle interface dynamics." International Journal of Machine Tools and Manufacture47.9 (2007): 1333-1341.

[19] Schmitz, Tony L., and G. Scott Duncan. "Receptance coupling for dynamics prediction of assemblies with coincident neutral axes." Journal of Sound and Vibration 289.4 (2006): 1045-1065.

[20] Schmitz, Tony L., et al. "Shrink fit tool holder connection stiffness/damping modeling for frequency response prediction in milling." International Journal of Machine Tools and Manufacture 47.9 (2007): 1368-1380.

[21] Filiz, S., et al. "An improved tool–holder model for RCSA tool-point frequency response prediction." Precision Engineering 33.1 (2009): 26-36.

[22] Budak, Erhan, A. Ertürk, and H. N. Özgüven. "A modeling approach for analysis and improvement of spindle-holder-tool assembly dynamics." CIRP Annals-Manufacturing Technology 55.1 (2006): 369-372.

[23] Ertürk, Alper, Erhan Budak, and H. Nevzat Özgüven. "Selection of design and operational parameters in spindle–holder–tool assemblies for maximum chatter stability by using a new analytical model." International Journal of Machine Tools and Manufacture 47.9 (2007): 1401-1409.

[24] Mancisidor, Iker, et al. "Receptance Coupling for Tool Point Dynamics Prediction." 17th CIRP International Conference on Modelling of Machining Operations. 2011.

[25] Duarte, Maria Lúcia M., and David J. Ewins. "Rotational degrees of freedom for structural coupling analysis via finite-difference technique with residual compensation." Mechanical Systems and Signal Processing 14.2 (2000): 205-227.

[26] Rezaei, Mohammad Mahdi, et al. "Extending the inverse receptance coupling method for prediction of tool-holder joint dynamics in milling." Journal of Manufacturing Processes 14.3 (2012): 199-207.

[27] Mehrpouya, Majid, Eldon Graham, and Simon S. Park. "FRF based joint dynamics modeling and identification." Mechanical Systems and Signal Processing 39.1 (2013): 265-279.

[28] Mehrpouya, M., M. Sanati, and S. S. Park. "Identification of joint dynamics in 3D structures through the inverse receptance coupling method." International Journal of Mechanical Sciences 105 (2016): 135-145.

[29] Montevecchi, F.,et al. "Improved RCSA technique for efficient tool-tip dynamics prediction." Precision Engineering 44 (2016): 152-162.

[30] Matthias, W., et al. "Receptance coupling based algorithm for the identification of contact parameters at holder–tool interface." CIRP Journal of Manufacturing Science and Technology 13 (2016): 37-45.

[31] Kumar, Uttara V., and Tony L. Schmitz. "Spindle dynamics identification for receptance coupling substructure analysis." Precision Engineering 36.3 (2012): 435-443.

[32] Ertürk, A., H. N. Özgüven, and Erhan Budak. "Effect analysis of bearing and interface dynamics on tool point FRF for chatter stability in machine tools by using a new analytical model for spindle–tool assemblies." International Journal of Machine Tools and Manufacture 47.1 (2007): 23-32.

[33] Yang, Yun, et al. "An improved method for tool point dynamics analysis using a bi-distributed joint interface model." International Journal of Mechanical Sciences 105 (2016): 239-252.

[34] Grossi, Niccolò, et al. "Speed-varying machine tool dynamics identification through chatter detection and receptance coupling." Procedia CIRP 55 (2016): 77-82.

[35] Zhang, Jun, et al. "Rapid dynamics prediction of tool point for bi-rotary head five-axis machine tool." Precision Engineering 48 (2017): 203-215.

[36] Yang, Yun, et al. "An improved method for tool point dynamics analysis using a bi-distributed joint interface model." International Journal of Mechanical Sciences 105 (2016): 239-252.

[37] Yang, Yun, et al. "Generalized method for the analysis of bending, torsional and axial receptances of tool–holder–spindle assembly." International Journal of Machine Tools and Manufacture 99 (2015): 48-67.

[38] Zhang, Jun, et al. "Rapid dynamics prediction of tool point for bi-rotary head five-axis machine tool." Precision Engineering 48 (2017): 203-215.

[39] Rahnama, Ramin, Mozhdeh Sajjadi, and Simon S. Park. "Chatter suppression in micro end milling with process damping." Journal of Materials Processing Technology 209.17 (2009): 5766-5776.

[40] Malekian, Mohammad, Simon S. Park, and Martin BG Jun. "Modeling of dynamic micro-milling cutting forces." International Journal of Machine Tools and Manufacture 49.7 (2009): 586-598.

[41] Park, S. S., and R. Rahnama. "Robust chatter stability in micro-milling operations." CIRP Annals-Manufacturing Technology 59.1 (2010): 391-394.

[42] Özşahin, Orkun, H. Nevzat Özgüven, and Erhan Budak. "Analysis and compensation of mass loading effect of accelerometers on tool point FRF measurements for chatter stability predictions." International Journal of Machine Tools and Manufacture 50.6 (2010): 585-589.

[43] Özgüven, H. Nevzat. "Structural modifications using frequency response functions." Mechanical Systems and Signal Processing 4.1 (1990): 53-63.

[44] Özşahin, Orkun, et al. "A closed-form approach for identification of dynamical contact parameters in spindle–holder–tool assemblies." International Journal of Machine Tools and Manufacture 49.1 (2009): 25-35.

[45] Schmitz, Tony L., and K. Scott Smith. Mechanical Vibrations: Modeling And Measurement. Springer Science & Business Media, 2011.

[46] Ganguly, Vasishta, and Tony L. Schmitz. "Phase correction for frequency response function measurements." Precision Engineering 38.2 (2014): 409-413.

[47] Kiran, Kadir, Harsha Satyanarayana, and Tony Schmitz. "Compensation of frequency response function measurements by inverse RCSA." International Journal of Machine Tools and Manufacture (2017).

[48] Schmitz, Tony L., and K. Scott Smith. Machining dynamics: frequency response to improved productivity. Springer Science & Business Media, 2008.